Quantum size effects of charge-transfer excitons in nonpolar molecular organic thin films

Zilan Shen and Stephen R. Forrest
Advanced Technology Center for Photonics and Optoelectronic Materials, Department of Electrical Engineering and Princeton Materials Institute, Princeton University, Princeton, New Jersey 08544
(Received 6 September 1996; revised manuscript received 19 December 1996)

We use a quantum-mechanical model to analyze charge-transfer (CT) excitons in closely packed, nonpolar organic molecular crystal thin films grown by the ultrahigh-vacuum process of organic molecular beam deposition. The exciton Hamiltonian includes both polarization effects and the periodic pseudopotential of the crystal. This model takes into account the very large anisotropy characteristic of many organic materials such as the archetype molecular crystal, 3,4,9,10-perylenetetracarboxylic dianhydride (PTCDA) and PTCDA-based multilayers. Using a single-exciton Hamiltonian, we quantitatively model experimental electroabsorption data and the absorption spectral shifts observed in ultrathin organic multilayers or ''multiple quantum wells.'' The data analyzed from several such experiments give independent and consistent estimations of the anisotropic effective mass tensor and exciton radii for PTCDA along different crystal axes. This treatment is general, and is found to extend to other CT and Wannier exciton systems found in many interesting, nonpolar organic molecular and inorganic semiconductor crystals such GaAs, suggesting similar physical origins for Wannier and CT excitons in a wide range of materials. [S0163-1829(97)07615-7]

I. INTRODUCTION

Excitons play a fundamental role in the optical properties of solids, and have been studied for many years beginning with the early experimental and theoretical work of Hilsch and Pohl,[1] Frenkel,[2] and Wannier.[3] The two extreme situations, the extended Wannier-Mott exciton and the localized Frenkel exciton, have been intensively investigated, and quantum-mechanical models have been developed to describe these fundamental excitations. In the first case, the Wannier-Mott exciton is based on a band structure arising from a significant overlap of crystalline periodic potentials. Assuming a single-electron model by applying the Hartree-Fock approximation, the Wannier-Mott exciton can be represented by an orthonormal complete set of hydrogenlike wave functions.[4–7] In the second case, the Frenkel exciton is considered as an intra-atomic or intramolecular excitation moving from site to site, with neither internal degrees of freedom nor internal quantum numbers. As a result of polarization of the electronic subsystems of the surrounding lattice due to charges and excitons, (i.e., many-body interactions), polaron-type quasiparticles are created. This renders the single-electron approximation inapplicable, and hence it is replaced by a Hamiltonian[8–10] that describes the Frenkel state by the exciton band number and wave vector. However, the internal quantum number of the Wannier exciton may in fact correspond to the Frenkel exciton band number, while such Frenkel excitons can be regarded as a limiting case of the Wannier state, where the relative electron-hole (e-h) motion is confirmed to a small region of atomic or molecular scale.[4]

The charge-transfer (CT) exciton is intermediate between these extremes, where the exciton is neither very extended nor tightly bound at a single molecular site. Since the concept of the CT exciton originates from the lowest excited state in crystals consisting of alternately arrayed donor and acceptor molecules (so-called ''donor-acceptor complexes''),[4] the CT state is usually considered as an unrelaxed polaron pair,[9] with both the positive and negative polarons of the charge pair localized on a set of discrete, identifiable, and nearly adjacent molecules.[11–13] The relaxed polaron state is called a charge pair state[9] or self-trapped CT exciton,[4,14] which is at an energy lower than CT states due to strong exciton-phonon coupling.

This localized picture is true only if each molecule is a point source of a δ-function-like potential. In that case, charges can only exist in a deep, narrow potential well at each nuclear or molecular site. In general, however, the charge is not static. Since the molecular ion has a finite size, shape, and orientation, the potential cannot be accurately modeled by a δ function. In addition, for planar stacking molecules where there is significant overlap between the π systems of adjacent molecules in the stack, the electronic states can no longer be considered as highly localized at a single lattice site. As a result, the exciton wave function must be an extended state, with its shape and symmetry intimately dependent on the crystalline and molecular structures.

In fact, extended CT states and quantum exciton confinement in organic thin films have already been proposed and observed.[14–18] For multilayer structures, or multiple quantum wells (MQW's) consisting of ultrathin layers of the planar stacking molecule 3,4,9,10-perylenetetracarboxylic dianhydride[19] (PTCDA, $C_{24}O_6H_8$) sandwiched between similar layers of 3,4,7,8-naphthalenetetracarboxylic dianhydride (NTCDA, $C_{14}O_6H_4$), it has been found that the energies of the exciton absorption peak[15] and the vibrational frequencies in the PTCDA fluorescence spectrum[16] increase with decreasing layer thickness. Recently, photoemission and inverse photoemission studies of PTCDA (Ref. 17) showed that the electron-hole exchange energy, which is the energy needed to remove an electron from one molecule and place it

on another, is[17] ~1 eV, or somewhat larger than the previously estimated molecular bandwidth of 0.1–0.4 eV.[14,21] This indicates the weak correlation as a direct result of charge delocalization in PTCDA. All of these results suggest that extended CT excitons are best described using quantum (extended) rather than electrostatic (localized) models typically applied to organic molecular crystals.[9]

In other experiments, photoluminescence and UV absorption spectra of self-assembled ultrathin films consisting of alternating layers of the conjugated copolymer, copoly(1,4-phenylenevinylene-1,4-napthylenevinylene), and the nonconjugated insulating polymer, poly(styrene-4-sulfonate), also indicate blueshifts upon decreasing the total thickness of the copolymer stacks.[18] As in the case of PTCDA, these self-assembled copolymer multilayers are found to stack facially, resulting in significant π-system overlap, and hence carrier delocalization, in the substrate-normal direction (i.e., perpendicular to the polymer chain axis). The observed spectral shifts for this system have been attributed to quantum confinement, where the exciton is ''squeezed'' in the potential well formed at the thin-film surfaces. Confinement, which results in an increase in exciton binding energy, was described using a model previously cited to explain similar phenomena in PTCDA-based multilayers.

Starting from the real space representation of chemical bonding, Mukamel and co-workers[22–26] proposed a second quantization approach to understand quantum size effects in ultrathin organic films. Their method was to map the electronic motions of the confined states onto a set of coupled harmonic oscillators. Based on the single-electron, reduced density matrix, and solving the time-dependent Hatree-Fock equation, the electronic charges and motion are then related to their optical response.[22] Using the Pariser-Parr-Pople tight-binding Hamiltonian for π electrons,[27] a basis set of exciton states is chosen to correspond to the discrete e-h separations, where each state is perturbed by Coulomb interactions, electron-electron coupling, lattice polarization, aggregate response, chemical bond oscillations, and interactions which induce the intermolecular charge transfer. The relative magnitudes of these terms determine the characteristics[23,24] of the exciton (i.e., whether it follows Frenkel, CT, or Wannier behavior). It was found[25] that quantum confinement of the relative (correlated) e-h motion of the CT exciton plays an important role in determining the magnitude of the third-order nonlinear susceptibility $\chi^{(3)}$ of conjugated polyenes. In addition, the lowest-lying absorption peak of poly(p-phenylene vinylene) oligomer[26] was calculated to redshift with respect to the isolated molecular absorption spectrum, which is very similar to the result observed by Bulovic *et al.*,[14] in solutions of PTCDA.

At low exciton densities where exciton-exciton coupling can be neglected, the self-consistent field approximation is valid. In this case, the e-h motion can be described by a quasiparticle interacting with an average field of the remaining charges. Based on this quasiparticle picture, the main goal of this work is to find a simple approach (i.e., a one-electron Hamiltonian) to describe the relatively delocalized CT exciton in anisotropic, nonpolar organic crystals, to study the effect of crystalline anisotropy on CT exciton energies, and to understand the experimental data such as ''quantum confinement'' in multilayer structures,[15] the electroabsorption (EA) spectra,[28] as well as other quantum phenomena frequently observed in nonpolar organic molecular crystals.[16,17] Furthermore, we show that our method is general, and can be used to describe EA spectra in inorganic semiconductors such as GaAs.[29,30]

This paper is divided into two main parts. In Sec. II, we calculate the polarization energies of an e-h pair in bulk organic crystals and alternating, lattice-matched multilayers such as MQW's. As an example, we calculate the polarization energies for closely packed, highly anisotropic, neutral molecular crystals such as PTCDA. Based on the quasimacroscopic e-h potential, we then write the effective one-exciton Hamiltonian. In Sec. III we study the effects of anisotropy on the quantum states and energies of CT excitons in organic molecular crystals such as PTCDA, and find that the lowest-energy CT exciton in this archetypal material is a nearly isotropic, hydrogenlike s state. By analyzing the EA data for PTCDA,[28] we estimate the effective-mass tensor and exciton radii along different crystal axes. We also fit the EA data of GaAs obtained by Miller *et al.*[29] and show that our treatment is indeed quite general. The absorption spectral shifts previously obtained in PTCDA/NTCDA multiple quantum wells[15] are also considered in the context of quantum size effects. This results in independent and consistent values for the effective masses and exciton radii as those obtained from the EA data. We briefly discuss the Stark shift in quantum-confined systems, and show that the CT spectral line broadening in an electric field can be minimized by choosing an optimized quantum-well thickness. Finally, in Sec. IV, we present conclusions. In the Appendix, we show details or the calculation of the screening of the external electric field (Appendix A 1), derive a mathematical expression treating the effective mass discontinuities in multilayer structures in Appendix A 2, and present an accurate variational method for calculating exciton radii and energies in quantum confined systems in Appendix A 3.

II. HAMILTONIAN AND POLARIZATION ENERGY OF NONPOLAR ORGANIC CRYSTALS

A. General treatment for anisotropic organic crystals

Due to the polarization of the surrounding medium in the presence of excess charges and excitations, the potential of an exciton state differs from that of an isolated molecular excited state by the crystal polarization energy.[31] Using classical electrostatics,[32] calculations of polarization energies, and therefore the interaction potentials of the e-h pair, were carried out by Jurgis and Silinsh using the self-consistent polarization field method,[32] and by Bounds and Siebrand[33] in terms of the Fourier-transformed lattice multipole sums. It was found that, to first order, the e-h interaction potential ($V_{e\text{-}h}$) is essentially Coulombic, e.g., $V_{e\text{-}h}=-q^2/\varepsilon_{\text{avg}}r$, for large charge pair separations, r (i.e., $r>$one lattice constant), where q is the charge, and ε_{avg} is the spatially averaged crystal dielectric constant. This result is, in some respects, similar to the case of conventional semiconductors, where the crystal lattice consisting of electrons and nuclei can be regarded[34] quasimacroscopically as a polarizable medium with a spatially averaged dielectric constant ε_{avg}, as long as the e-h distance is large compared to the lattice constant. Fundamentally, an electron in the conduction band, or the

lowest unoccupied molecular orbital (LUMO), as well as a hole in the valence band, or the highest occupied molecular orbital (HOMO), are always accompanied[35,36] by electronic polarization (via polarons) of the surrounding medium. This similarity suggests the feasibility of applying the Wannier exciton model to describe CT excitons with radii larger than one lattice constant.

In this work, PTCDA is studied because of its important role in understanding the fundamental properties of CT excitons, its promising optoelectronic properties,[37–41] and the numerous investigations[14–17,28,37–41] which have provided accurate optical data. Our treatment for calculating the crystal polarization due to excess charges is similar in most respects to the method of Bounds, and co-workers,[12,13] although it differs in the calculation of the effective polarizability for highly anisotropic crystals such as PTCDA. Polarization energy is thus calculated to determine analytically a continuous, quasimacroscopic potential with a position-dependent effective dielectric tensor. From this analysis, we write the effective one-exciton Hamiltonian, and hence determine the energies and wave functions of CT excitons by solving Schrödinger's equation.

For a lattice with a basis whose unit-cell volume is ν, the molecular position is defined by $\mathbf{r}(lk)$, where $l=\{l_x,l_y,l_z\}$ is the lattice index, and $k=\{1,2,3\ldots\}$ is the index of a particular basis molecule within the unit cell. Due to the external electric field $\mathbf{F}_0$ of the excess charges in the crystal, the medium is polarized. The macroscopic field $\mathbf{F}_{\rm mac}$ at site (l,k) thus includes $\mathbf{F}_0$ and the induced dipole field, $\mathbf{F}_{\rm ind}$, via

$$\mathbf{F}_{\rm mac}(lk)=\mathbf{F}_0(lk)+\mathbf{F}_{\rm ind}(lk), \tag{1}$$

where $\mathbf{F}_{\rm ind}$ is the sum of two terms: the field due to the dipole at the same site (self-field, $\mathbf{F}_{\rm self}$), and the field due to the surrounding dipoles

$$\mathbf{F}_{\rm ind}(lk)=\mathbf{F}_{\rm self}(lk)+\sum_{l'k'\neq lk}\mathbf{t}(lk,l'k')\cdot\boldsymbol{\mu}(l'k'). \tag{2}$$

Assuming a spherical dipole for homogeneous and isotropic media, $\mathbf{F}_{\rm self}$ is usually taken as $-\boldsymbol{\mu}(lk)/3\nu\varepsilon_0$,[42] where ε_0 is the vacuum permittivity. Here $\mathbf{t}$ is the dipole tensor

$$\mathbf{t}(lk,l'k')=\lim_{r\to r(l',k')}\nabla\nabla|\mathbf{r}(lk)-\mathbf{r}|^{-1}, \tag{3a}$$

and $\boldsymbol{\mu}$ is the induced dipole moment

$$\boldsymbol{\mu}(lk)=\overleftrightarrow{\alpha}(k)\cdot\mathbf{F}_{\rm loc}(lk), \tag{3b}$$

where $\overleftrightarrow{\alpha}(k)$ is the effective polarizability of molecule k, and the local field $\mathbf{F}_{\rm loc}(lk)$ is the average field at site (l,k) excluding the induced field due to molecule (l,k). Hence

$$\mathbf{F}_{\rm loc}(lk)=\mathbf{F}_{\rm mac}(lk)-\mathbf{F}_{\rm self}(lk). \tag{4}$$

Equations (1)–(4) give

$$\boldsymbol{\mu}(lk)=\overleftrightarrow{\alpha}(k)\cdot\left[\mathbf{F}_0(lk)+\sum_{l'k'\neq lk}\mathbf{t}(lk,l'k')\cdot\boldsymbol{\mu}(l'k')\right]. \tag{5}$$

From Eq. (5), the induced dipole moment in Fourier space is therefore[33]

$$\boldsymbol{\mu}(\mathbf{y},k)=\overleftrightarrow{\alpha}(k)\cdot\left[\mathbf{F}_0(\mathbf{y},k)+\sum_{k''}\mathbf{t}(\mathbf{y},kk')\cdot\boldsymbol{\mu}(\mathbf{y},k')\right], \tag{6}$$

where $\mathbf{y}$ is the reciprocal displacement vector. Introducing supervector $\widetilde{\mathbf{Q}}_k(y)=\mathbf{Q}(y,k)$, and supermatrix $\widetilde{\mathcal{R}}_{kk'}(\mathbf{y})=\overleftrightarrow{\mathcal{R}}(\mathbf{y},kk')$, and defining the unit matrix $\mathbf{I}$, we have

$$\widetilde{\mu}(\mathbf{y})=[\mathbf{I}-\widetilde{\alpha}\cdot\widetilde{\mathbf{t}}(y)]^{-1}\cdot\widetilde{\alpha}\cdot\widetilde{\mathbf{F}}_0(y)=\widetilde{\Theta}(\mathbf{y})\widetilde{\mathbf{F}}_0(\mathbf{y}). \tag{7}$$

To evaluate $\widetilde{\Theta}(\mathbf{y})=[\widetilde{\alpha}^{-1}-\widetilde{\mathbf{t}}(\mathbf{y})]^{-1}$, we use Maxwell's equation $\nabla\cdot[\mathbf{F}_{\rm mac}(\mathbf{r})+4\pi\mathbf{P}(\mathbf{r})]=\rho(\mathbf{r})$, where ρ is the excess charge density, and $\mathbf{P}=\Sigma_k\boldsymbol{\mu}(lk)/\nu$ is the polarization vector. The macroscopic field $\mathbf{F}_{\rm mac}$ and the external field $\mathbf{F}_0$ (Ref. 43) are then related via

$$\mathbf{F}_{\rm mac}(\mathbf{y},k)=\mathbf{F}_0(\mathbf{y},k)-\frac{4\pi}{\nu}\left(\frac{\mathbf{y}}{|\mathbf{y}|}\right)\left(\frac{\mathbf{y}\cdot\boldsymbol{\mu}(\mathbf{y},k)}{|\mathbf{y}|}\right), \tag{8}$$

where the second term on the right is, in fact, $\mathbf{F}_{\rm ind}(\mathbf{y},k)$.

In the long-wavelength limit ($\mathbf{y}\to0$), which corresponds to the region near the origin of the first Brillouin zone, the constitutive relation gives

$$\mathbf{P}=\boldsymbol{\mu}(\mathbf{y}\to0)/\nu=\overleftrightarrow{\chi}\mathbf{F}_{\rm mac}(\mathbf{y}\to0), \tag{9}$$

where $\overleftrightarrow{\chi}$ is the macroscopic susceptibility, $\overleftrightarrow{\chi}=(\overleftrightarrow{\varepsilon}_r-I)/4\pi$, and $\overleftrightarrow{\varepsilon}_r$ is the macroscopic dielectric tensor. Using the Lorentz-factor tensor[44] $\widetilde{\mathbf{L}}=\lim_{\mathbf{y}\to0}[\widetilde{\mathbf{t}}(\mathbf{y})+4\pi\widetilde{\mathbf{y}}\,\widetilde{\mathbf{y}}^{\rm T}/|\mathbf{y}|^2\nu]$, we then rewrite Eq. (8) as

$$\widetilde{\mathbf{F}}_{\rm mac}(\mathbf{y}\to0)=[\overleftrightarrow{\alpha}^{-1}-\widetilde{\mathbf{L}}]\widetilde{\mu}(\mathbf{y}\to0). \tag{10}$$

Note that Eq. (10) differs somewhat from previous solutions proposed by Dunmur and co-workers,[44,45] and employed by Cummins and co-workers[44] in the case of anthracene, etc. That work only dealt with the position-independent field in real space, which can lead to errors in treating a crystal with a basis. For cases where the basis molecules do not have the same polarizability, one should not expect both $\mathbf{F}_{\rm mac}$ and $\mathbf{P}$ to have a single average value across the entire unit cell. Therefore, we introduce the average polarization within the basis at site k as

$$\mathbf{P}(\mathbf{y}\to0,k)=(1/\nu_k)\boldsymbol{\mu}(\mathbf{y}\to0,k)=\overleftrightarrow{\chi}\mathbf{F}_{\rm mac}(\mathbf{y}\to0,k). \tag{11}$$

Here ν_k is the volume that molecule k occupies (e.g., $\nu_k=\nu/Z$ for homogeneous crystals with Z basis molecules per unit cell). Thus

$$\widetilde{\mathbf{F}}(\mathbf{y})=(1/\nu_k\varepsilon_0)\widetilde{\chi}^{-1}\widetilde{\mu}(\mathbf{y}), \tag{12}$$

where we define the supermatrix $\widetilde{\chi}_{kk'}=(\nu/\nu_k)\overleftrightarrow{\chi}\delta_{kk'}$. Comparing Eqs. (10) and (12) gives

$$\overleftrightarrow{\alpha}^{-1}=\widetilde{\chi}^{-1}+\widetilde{\mathbf{L}}, \tag{13a}$$

and, for every $\mathbf{y}$,

$$\widetilde{\Theta}(y)=[\widetilde{\chi}^{-1}+\widetilde{\mathbf{L}}-\widetilde{\mathbf{t}}(\mathbf{y})]^{-1}. \tag{13b}$$

Hence $\widetilde{\Theta}(\mathbf{y})$ can be regarded as the effective polarizability of the crystal due to the dipole interactions. Using Eq. (13b), the polarization response of the crystal in Fourier space is

$$p_E(\mathbf{y})=\widetilde{\mathbf{F}}_0(-\mathbf{y})^T\cdot\widetilde{\mu}(\mathbf{y})=\widetilde{\mathbf{F}}_0(-\mathbf{y})^T\cdot\widetilde{\Theta}(\mathbf{y})\cdot\widetilde{\mathbf{F}}_0(\mathbf{y}). \tag{14}$$

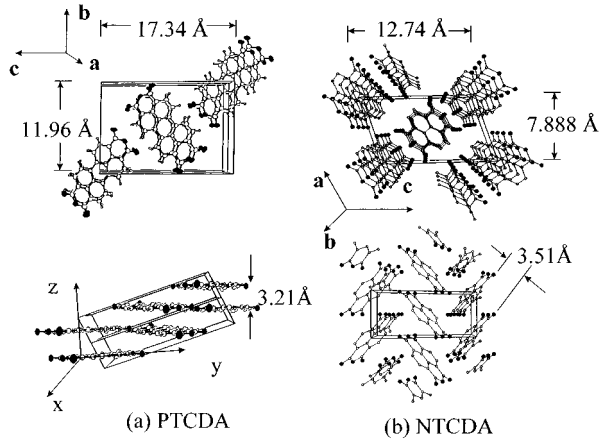

FIG. 1. Perspective views of the unit cells of (a) PTCDA and (b) NTCDA, and the orientation of PTCDA crystal axes with respect to the substrate. The planar molecules of PTCDA films form stacks in the (102) plane which lie parallel to the substrate plane, and z is the substrate normal direction.

The total polarization energy, P_E, is the integration of $p_E(\mathbf{y})$ over the first Brillouin zone,

$$P_E = -\tfrac{1}{2}\sum_{lk} \tilde{\mathbf{F}}_0(lk)\cdot\boldsymbol{\mu}(lk) = -\nu/2\int_{1\mathrm{BZ}} p_E(\mathbf{y})dy. \quad (15)$$

Thus the potential energy of an e-h pair in a nonpolar organic crystal is a sum of the unscreened Coulomb attraction and the microscopic lattice response to the existing e-h pair in terms of the polarization energy, via

$$V_{e\text{-}h} = -\frac{q^2}{|\mathbf{r}(l_1k_1,l_2k_2)|} + P_E[\mathbf{r}(l_1k_1,l_2k_2)]. \quad (16)$$

B. Polarization energies for NTCDA and PTCDA

We now use Eq. (16) to calculate e-h interaction energies in the archetypal materials NTCDA and PTCDA. In Fig. 1, we show the structural formulas and two views of the unit cells (space group $P2_1/c$) for bulk crystals of NTCDA and PTCDA as characterized by x-ray diffraction.[46,47] The values of their primitive vectors **a**, **b**, and **c** and other crystal properties are listed in Table I.

The PTCDA molecules stack facially in the (102) plane, which can either lie parallel to, or tilted at 11° from the substrate plane,[46,47] and have a stacking distance of only 3.21 Å. This unusually small intermolecular separation leads to a significant degree of charge delocalization along the (102) stacking axis, resulting in large anisotropies in crystalline properties along various axes. In this respect, PTCDA becomes an ideal system in which to test assumptions leading to the potential given in Eq. (16).

TABLE I. Lattice parameters, average dielectric constants, and HOMO-LUMO energy gaps (E_g) of PTCDA and NTCDA.

	a (Å)	b (Å)	c (Å)	β	$\varepsilon_{\mathrm{avg}}$	E_g (eV)
PTCDA	3.719	11.96	17.34	98.81°	3.23	2.2
NTCDA	7.888	5.334	12.74	109.04°	2.6	3.1

TABLE II. Dielectric tensor elements for PTCDA.

	aa	bb	cc	aa'	ac	ab	bc	$\perp$	$\parallel$
ε	2.1	4.5	4.3	2.4	−0.9	0.0	0.0	1.9	4.5

Taking z as the substrate normal axis, the dielectric tensor elements of PTCDA have previously been measured,[48] where $\varepsilon_z = 1.9$, and $\varepsilon_x = \varepsilon_y = 4.5$. This results in the dielectric constants along principal axes of $\varepsilon_\perp = 1.9$ and $\varepsilon_\parallel = 4.5$, where $\perp$ denotes the (102) stacking direction of the molecules, and $\parallel$ is in the molecular plane. From the crystal structure, the dielectric tensor elements can be calculated with respect to the lattice primitive vectors, and are listed in Table II.

The crystalline and dielectric anisotropies of NTCDA are much smaller than for PTCDA due to the herringbone stacking habit, as shown in Fig. 1(b). In previous work, the spacing between molecular planes was found to be 3.506 Å,[41] and the index of refraction was found[49] to be nearly isotropic, at $n = 1.6$. Thus we assume an isotropic dielectric constant $\varepsilon_{\mathrm{avg}} \approx 2.6$.

The interaction energy $V_{e\text{-}h}$ as a function of e-h separation, $r = |\mathbf{r}|$, has been calculated for both NTCDA (Fig. 2), and PTCDA (Fig. 3). The results are compared with the ''screened'' Coulomb potential $V_{\mathrm{scr}} = -q^2/|\vec{\varepsilon}\cdot\mathbf{r}|$, where ε is the macroscopic dielectric tensor for the crystal. We find that, for NTCDA, the ''screened'' potential $V_{\mathrm{scr}} = -q^2/\varepsilon_{\mathrm{avg}} r$ gives a good fit to our calculations along each crystalline axis. In calculating the polarization energies, the integral over $\mathbf{y}$ in the first Brillouin zone [Eq. (15)] is segmented into a summation of G grid elements. Since $p_E(\mathbf{y})$ diverges in the long-wavelength limit[12] ($\mathbf{y}\to 0$), the summation is separated into two parts for calculation convenience, i.e., $P_E = P_0(\mathbf{y}\to 0) + P_1(\mathbf{y}\neq 0)$. The inset of Fig. 2 plots P_0, P_1, and

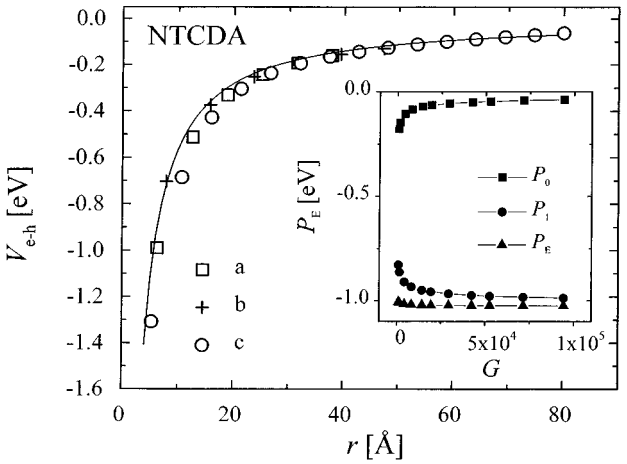

FIG. 2. Electron-hole potential energy ($V_{e\text{-}h}$) calculated for NTCDA as a function of charge separation (r) along three crystalline axes (data points). Since NTCDA has an isotropic dielectric tensor, the calculation is compared with results obtained in the isotropic continuum approximation, where $\varepsilon = 2.6$ (solid line). Inset: The polarization energy P_E of one charge in the crystal as a function of summation grid number G. The convergence at $G > 2\times 10^4$ suggests the calculation is a good approximation to the integration over $\mathbf{y}$.

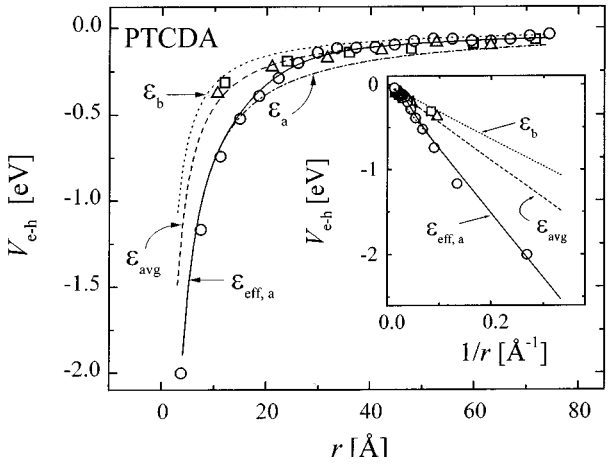

FIG. 3. Electron-hole potential energy ($V_{e\text{-}h}$) calculated for PTCDA as functions of charge separation r along three crystalline axes (**a** axis, circles; **b** axis, squares; **c** axis, triangles). The dash-dotted curve is $V_{e\text{-}h} \approx V_{scr}$ using the dielectric constant along the **a** axis, $\varepsilon_a = 2.1$, and the dotted curve uses the value along the **b** and **c**, $\varepsilon_b = 4.5$ (where $\varepsilon_b \approx \varepsilon_c$). The dashed curve uses the spatial averaged dielectric constant $\varepsilon_{avg} = 3.2$. Note when $r > 25$ Å, ε_{avg} results in the best fit, and when $r < 15$ Å, then ε_i (where i represents the crystalline axes), provides an excellent approximation to the calculated values. The solid curve uses the effective dielectric constant ε_{eff} described in text [Eq. (18)]. Inset: $V_{e\text{-}h}$ data replotted as functions of $1/r$.

the total polarization energy P_E for one charge in the crystal as a function of G. We find that P_E converges for $G \geqslant 10^4$.

The results are considerably different for PTCDA, where $V_{e\text{-}h}$ depends rather sensitively on the direction of **r** for small $e\text{-}h$ separations. In Fig. 3, the dashed curve represents $V_{scr} = -q^2/\varepsilon_{avg} r$, where $\varepsilon_{avg} = 3/(1/\varepsilon_\perp + 2/\varepsilon_\parallel) = 3.2$ is the spatially averaged permittivity [Eq. (A7), Appendix A 1]. Using ε_{avg} results in the best fit to $V_{e\text{-}h}$ for large r (>25 Å), regardless of crystalline direction. That is, even for anisotropic systems such as PTCDA, the potential becomes spatially averaged at distances of only a few molecular lattice constants from the origin. However, for small r (<15 Å), $V_{e\text{-}h}$ deviates significantly from the spatial average. This deviation is again clearly shown in the inset of Fig. 3, where $V_{e\text{-}h}$ is plotted as a function of $1/r$. In this region of small r, we find that the mean dielectric constant approximation $V_{scr} = -q^2/\varepsilon_i r$ (where i refers to crystalline directions) provides a good fit to $V_{e\text{-}h}$, as shown by the corresponding curves in Fig. 3.

To accurately approximate the $e\text{-}h$ interaction energy for all **r** of anisotropic systems such as PTCDA we replace Eq. (16) with the ''screened Coulomb potential''

$$V_{e\text{-}h} \approx V_{scr} = -q^2/|\vec{\varepsilon}_{eff}(\mathbf{r}) \cdot \mathbf{r}| \tag{17}$$

where $\vec{\varepsilon}_{eff}(\mathbf{r})$ is the position-dependent effective dielectric tensor, whose diagonalized elements are given by

$$\varepsilon_{eff,i}(r) = \varepsilon_i + A\{\tanh[(r^2 - r_0^2)/4r_0^2] + B\}, \tag{18}$$

where, for PTCDA, $r_0 = 10$ Å is the ''transition radius'' between microscopic and macroscopic behavior, $B = \tanh(r_0^2/4r_0^2) \approx 4.08$, and $A = (\varepsilon_{avg} - \varepsilon_i)/(1+B)$, such that $\varepsilon_{eff,i}(r < r_0) = \varepsilon_i$ and $\varepsilon_{eff,i}(r > 3r_0) = \varepsilon_{avg}$. Figure 3 provides a plot of Eq. (17) along the **a** axis, where we find the approximation is remarkably accurate with a maximum error of less than 20 meV over all **r**. In Sec. III, we will study the effects of a small deviation of the $e\text{-}h$ potential on the exciton energy, and will show that Eqs. (17) and (18) are indeed an excellent approximation at all **r**.

For lattice-matched multilayer structures, $V_{e\text{-}h}$ can also be calculated using the same treatment. Choosing the unit cell to cover one period of the superlattice consisting of $J = J_1 + J_2$ monolayers, where J_1 is the number of monolayers of material i, the volume of the unit cell is then $\nu = \nu_1 J_1 + \nu_2 J_2$, where ν_i is the volume of the unit cell for material i. Supermatrix $\tilde{\chi}$ in Eq. (13b) is thus $\tilde{\chi}_{kj,k'j'} = (\nu/\nu_{kj})\vec{\chi}_j \delta_{kk'} \delta_{jj'}$, where $j = 1,\ldots,J$, $\vec{\chi}_j = \vec{\chi}_1$ for $j \leqslant J_1$, and $\vec{\chi}_j = \vec{\chi}_2$ for $j > J_1$.

The $e\text{-}h$ interaction energy has been calculated for $J_1 = J_2 = 1$, where Eqs. (17) and (18) can be used to approximate $V_{e\text{-}h}$ by taking $\varepsilon_{eff}(\mathbf{r}) = [\Sigma_{i=1,2} \nu_i g_{eff,i}^3(\mathbf{r})/\nu]^{1/3}$. For J_1, $J_2 \geqslant 3$, the potential reaches the spatially averaged limit (see, for example, Figs. 2 and 3), and the result used for homogeneous material layers discussed previously is sufficient to calculate the polarization energy in such organic multilayers.

Note that screening of the Coulomb potential as suggested by Eqs. (17) and (18) is also typical for most inorganic semiconductors.[4] In that case, however, electrons make the most significant contribution to electric-field screening, (leading to $r_0 \approx 3-4$ Å), whereas, for organic crystals, screening arises primarily from the molecular polarization, which diminishes for small **r** (with $r_0 \approx 10$ Å).

C. Hamiltonian for CT exciton states

For semiconductors with a large overlap of atomic wave functions between ionic cores in the crystal, the periodic pseudopotential (V_{pseudo}) applied on the valence electrons is weak enough to result in a modified free-electron gas. In this limit, the motion of the electron can be described by the one-electron Schrödinger's equation, leading to a description of the energy levels in terms of a family of continuous functions $E_n(\mathbf{k})$, each with the periodicity of the reciprocal lattice. This results in a bond structure, where n refers to the energy band, and **k** is the conserved crystal momentum. This small lattice periodic pseudopotential V_{pseudo} leads to relatively high carrier mobility ($\geqslant 0.01$ cm^2/V s), and wide energy bands (electron-hole exchange energy, V_{exc}). Figure 4(a) shows a schematic representation of $V_{e\text{-}h}$, and the total ''delocalized'' exciton potential $V_{deloc} = V_{e\text{-}h} + V_{pseudo}$, typical of ionic or covalently bonded materials such as Si or GaAs. Under such conditions, the exciton states are hydrogenic, where the lowest-energy (s-like) state wave-function density $(\varphi^* \varphi)_{deloc}$, is also plotted in Fig. 4(a).

In contrast, organic molecular crystals are typically characterized by weak intermolecular van der Waals (vdW) interactions, with a bonding energy considerably less than that of covalent or ionic bonds in atomic crystals. This often leads to a relatively small overlap of molecular orbitals, and hence a strong localization of excess charge carriers. Under such conditions, both the one-electron approximation and the concept of extended energy bands become questionable. Additionally, elastic and inelastic interactions between the charge carrier and lattice are strongly coupled, such that the

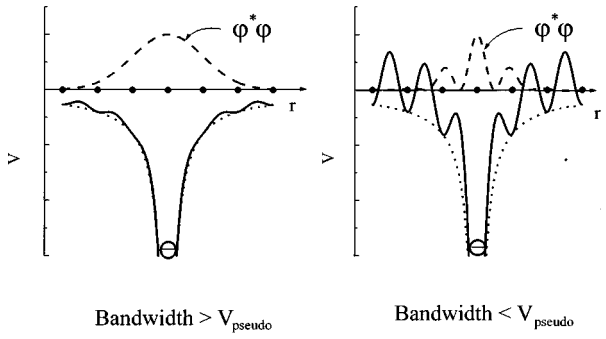

FIG. 4. (a) Schematic diagram showing $V_{e\text{-}h}$ (dotted line), the total potential $V_{e\text{-}h}+V_{\text{pseudo}}$ (solid line), and $\varphi^*\varphi$ as a function r for a delocalized exciton. (b) $V_{e\text{-}h}$, the total potential $V_{e\text{-}h}+V_{\text{pseudo}}$, and $\varphi^*\varphi$ as a function r for a localized exciton.

wave momentum $\mathbf{k}$ is not conserved, thus further increasing charge localization.[50] For this case, V_{pseudo} is large, and comparable in magnitude to $V_{e\text{-}h}$. Here V_{pseudo} corresponds to the on-site correlation energy which approximately equals the difference between the electron-hole exchange energy, V_{exc}, and P_E. This is characteristic of many vdW solids, leading to a low charge carrier mobility ($\leqslant 10^{-4}$ cm^2/V s) and narrow energy bands.[51] Figure 4(b) shows the total potential V_{loc} for such media where the e-h pair is localized on the molecular sites. The resulting wave function density $(\varphi^*\varphi)_{\text{loc}}$ is also plotted in Fig. 4(b). Anthracene and the phthalocyanines are materials typical of this class of molecular crystals. In fact, the calculated band structure shows that electronic polarization effects reduce the effective bandwidth in anthracene[50] by 50%. The resulting electron mean free path is found to be smaller than the intermolecular spacing, demonstrating the inconsistency of the band model for anthracene-type crystals.

Nevertheless, for some molecular crystals, where there is significant overlap between the π systems of closely stacked adjacent molecules, the energy bandwidth is comparable to or larger than V_{pseudo},[22] while the mean free path can be comparable to or greater than the intermolecular spacing, leading to significantly delocalized charge carriers. Since the electronic polarization time constant is very short (10^{-16}–10^{-15} s),[9] the one-electron model might still apply, with the exact form and magnitude of V_{pseudo} depending on the crystal structure, the unit-cell basis, and the degree of overlap of the intermolecular π orbitals.

Given the unusually small intermolecular distance in PTCDA, which leads to a high hole mobility ($\sim$1 cm^2/V s) along the stacking direction, spatially extended CT states[15,28] with large ($\sim$1) oscillator strengths, and a total ''bandwidth'' of 0.1–0.4 eV (Ref. 20), comparable to $V_{\text{pseudo}}\sim 0.5$ eV. Here, we use the measured[17] value for V_{exc} ($\sim$1 eV), and the calculated $P_E=1.5$ eV for PTCDA, along with $V_{\text{pseudo}}=|V_{\text{exc}}-P_E|$. Thus we infer that, in the case of PTCDA and similarly ''large bandwidth'' vdW solids, V_{pseudo} can be neglected. Following the treatment in Sec. II B, the Hamiltonian for such delocalized CT excitons in the center-of-mass coordinates is thus[6]

$$H_0=T+V_{e\text{-}h}+V_{\text{pseudo}}\cong-\frac{\hbar^2}{2}\left(\frac{\nabla_{\parallel}^2}{m_{\parallel}}+\frac{\partial_{\perp}^2}{m_{\perp}}\right)-\frac{q^2}{r}+P_E(\mathbf{r}). \tag{19}$$

Here $\mathbf{r}=\mathbf{r}_e-\mathbf{r}_h$ is the displacement vector of the e-h pair, T is the kinetic energy, $m_i=m_{e,i}m_{h,i}/(m_{e,i}+m_{h,i})$ is the reduced effective mass along direction $i=\perp$ or $\parallel$, m_e (m_h) is the effective electron (hole) mass, and $\hbar$ is the Planck's constant divided by 2π. For PTCDA, we approximate $\perp$ to be along the substrate normal, z.[47] As in Sec. II B, the last two terms can be replaced by Eqs. (17) and (18) for an excellent approximation.

III. EXCITONS AND QUANTUM SIZE EFFECTS

A. Free-exciton wave function and energy

To treat the dielectric and mass anisotropies in solving Eq. (19), cylindrical coordinates $\mathbf{r}=(\rho,\phi,z)$ are used to reflect the nearly isotropic nature of PTCDA in $\parallel$ directions (ρ,ϕ), and the significant anisotropy in the $\perp$ direction (z). To incorporate the mass anisotropy, we use the unitless coordinates $\mathbf{r}'=(\rho',\phi',z')$, such that $\rho=b_{\parallel}\rho'$, $\phi=\phi'$, and $z=b_{\perp}z'$, where b_i is the length unit, $b_i=a_b\varepsilon_{\text{avg}}\sqrt{m_0/m_i}$, $a_b=\hbar^2/m_0q^2=0.529$ Å is the Bohr radius of the free electron, and m_0 is the free-electron mass. The energy unit is Ryd/$\varepsilon_{\text{avg}}^2$, where Ryd$=q^2/2a_b=13.6$ eV. The reduced Hamiltonian becomes

$$h_0=\frac{H_0}{\text{Ryd}/\varepsilon_{\text{avg}}^2}=-\nabla_{r'}^2-\frac{2}{\sqrt{\beta_{\parallel}^2\rho'^2+\beta_{\perp}^2z'^2}}, \tag{20a}$$

where the anisotropy of the crystal is expressed by

$$\beta_i=\sqrt{m_i/m_0}\,\varepsilon_{\text{avg}}/\varepsilon_i. \tag{20b}$$

Thus, in reduced coordinates, the kinetic-energy operator is isotropic, where the anisotropic mass and dielectric tensor elements are contained in β_i. Focusing on the lowest, $1s$ exciton state, we choose the trial wave function[52]

$$\varphi_{1s}=\exp(-g)/\sqrt{\pi c_{\parallel}^2c_{\perp}}, \tag{21a}$$

where

$$g=(\rho'^2/c_{\parallel}^2+z'^2/c_{\perp}^2)^{1/2}. \tag{21b}$$

Here $c_{\parallel}$ and $c_{\perp}$ are variational parameters used to minimize energy, where $c_{\perp}/c_{\parallel}$ describes the resulting asymmetry of the wave function. The lowest energy $\overline{E_{1s}^{(0)}}$ is found via $\overline{E_{1s}^{(0)}}(\overline{c_{\parallel}},\overline{c_{\perp}})=\min_{c_{\parallel},c_{\perp}}[E(c_{\parallel},c_{\perp})]=\min_{c_{\parallel},c_{\perp}}\langle\varphi_{1s}|H_0|\varphi_{1s}\rangle$, and the exciton radius along i is then $\overline{a_i}=b_i\overline{c_i}=a_b\overline{c_i}\varepsilon_{\text{avg}}\sqrt{m_0/m_i}$.

To show how anisotropies in the dielectric tensor can distort the $1s$ state, in Fig. 5 we plot $\overline{a_{\perp}}$ and $\overline{a_{\parallel}}$ as functions of the anisotropy parameter $\beta_{\parallel}/\beta_{\perp}$ for $m_{\perp}=m_{\parallel}=018m_0$, and $\varepsilon_{\text{avg}}=3.23$. In this case of $m_{\perp}=m_{\parallel}$, then $\beta_{\parallel}/\beta_{\perp}=\varepsilon_{\perp}/\varepsilon_{\parallel}$. Thus, for $\varepsilon_{\perp}<\varepsilon_{\parallel}$, we find $\overline{a_{\perp}}>\overline{a_{\parallel}}$, and vice versa. That is, $\overline{a_i}$ scales inversely as ε_i, leading to asymmetries in the s state. To include the effects of mass anisotropy, we plot the ratio of exciton radii in reduced units $\overline{c_{\perp}}/\overline{c_{\parallel}}$ as a function of $\beta_{\parallel}/\beta_{\perp}$ in the inset of Fig. 5. Obviously, when $\beta_{\perp}=\beta_{\parallel}$, the wave function is spherical, leading to $\overline{c_{\perp}}=\overline{c_{\parallel}}$ (i.e., $\overline{a_{\perp}}/\overline{a_{\parallel}}=\sqrt{m_{\parallel}/m_{\perp}}$). In this case, the $1s$ state energy is $\overline{E_{1s}^{(0)}}=\text{Ryd}\,\beta_{\perp}^2/\varepsilon_{\text{avg}}^2$.

On the other hand, anisotropic potentials ($\beta_{\parallel}\neq\beta_{\perp}$) result in anisotropic exciton radii ($\overline{c_{\parallel}}\neq\overline{c_{\perp}}$). Once again, for small $\beta_{\parallel}/\beta_{\perp}$, the radius along $\perp$ is larger than that along $\parallel$, giving

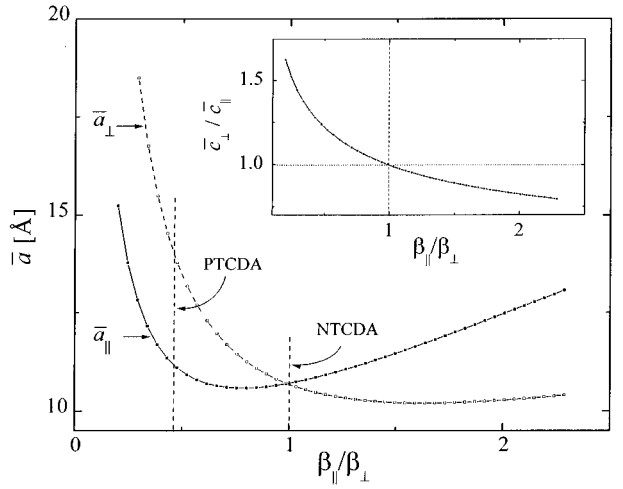

FIG. 5. Exciton radii $\overline{a_\perp}$ and $\overline{a_\parallel}$, as functions of the reduced anisotropy parameters $\beta_\parallel/\beta_\perp$ for $m_\perp = m_\parallel = 0.16m_0$. The spatially averaged dielectric constant is fixed at $\varepsilon_{avg}=3.23$. In this plot, $\beta_\parallel/\beta_\perp = \varepsilon_\perp/\varepsilon_\parallel$. The vertical lines indicate the anisotropies characteristic of PTCDA and NTCDA. Inset: Reduced exciton radii $c_\perp/c_\parallel$ as a function of anisotropy $\beta_\parallel/\beta_\perp$.

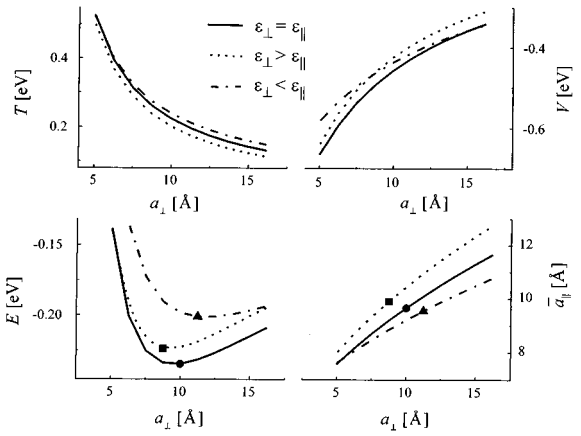

FIG. 6. Kinetic (T), potential (V), and total (E_{1s}) energies, and in-plane radius ($\overline{a_\parallel}$) as functions of $a_\perp$ for isotropic ($\epsilon_\perp = \epsilon_\parallel = 3.23$) and anisotropic ($\epsilon_\perp = 2.2$, $\epsilon_\parallel = 4.2$, dotted curves; $\epsilon_\perp = 4.5$, $\epsilon_\parallel = 2.9$, dashed-dotted curves) dielectric tensors. For these curves, the energy is minimized with respect to $a_\parallel$, taking $m_\parallel = m_\perp = 0.18m_0$ and $\varepsilon_{avg}=3.23$. The symbols correspond to values obtained at the minimum energy with respect to both $a_\parallel$ and $a_\perp$.

$\overline{c_\perp} > \overline{c_\parallel}$. This result at first appears to be unexpected, since a smaller radius is anticipated in the direction where ε is smaller, or m is larger. To understand this apparent contradiction, in Fig. 6 we plot the kinetic energy (T), the potential energy (V), the total exciton $1s$ state energy (E_1), and $\overline{a_\parallel}$ as functions of $a_\perp$ for three cases: $\epsilon_\perp = \epsilon_\parallel = 3.23$; $\epsilon_\perp = 2.2$ and $\epsilon_\parallel = 4.2$; and $\epsilon_\perp = 4.5$ and $\epsilon_\parallel = 2.9$, using[15] $m_\parallel = m_\perp = 0.18m_0$, and $\varepsilon_{avg}=3.23$. For each $a_\perp$, E_{1s} is minimized with respect to $a_\parallel$. We find that isotropic media ($\epsilon_\perp = \epsilon_\parallel$) have the lowest $1s$ state energy. For $\epsilon_\perp < \epsilon_\parallel$, the potential energy has a weaker dependence on $a_\perp$ as compared to the isotropic case, while the kinetic energy maintains a similar dependence. Therefore the minimum energy is located at larger $a_\perp$, as inferred from Fig. 6.

The inset of Fig. 7 is a plot of $E_{1s}^{(0)}(a_\parallel, a_\perp)$ as a function of $a_\parallel$ and $a_\perp$, using[15] $m_\parallel = m_\perp = 0.18m_0$, and $V_{e\text{-}h}$ as calculated in Sec. II. The minimum value $\overline{E_{1s}^{(0)}} = (191 \pm 20)$ meV is obtained for $\overline{a_\parallel} = (9.8 \pm 0.3)$ Å and $\overline{a_\perp} = (12.5 \pm 0.2)$ Å. As expected, the exciton radius is larger along $\perp$, where the close molecular stacking for PTCDA leads to pronounced wave-function delocalization as compared with that along $\parallel$. Fixing the spatially averaged dielectric constant at $\varepsilon_{avg}=3.23$, we plot $\overline{E_{1s}^{(0)}}$ in Fig. 7 as functions of $\beta_\parallel/\beta_\perp$ for three different effective-mass tensors (solid line: $m_\parallel = 0.16m_0$ and $m_\perp = 0.16m_0$; dashed line: $m_\parallel = 0.26m_0$ and $m_\perp = 0.16m_0$; dotted line: $m_\parallel = 0.40m_0$ and $m_\perp = 0.10m_0$). We find that $E_{1s}^{(0)}$ increases when $\beta_\parallel/\beta_\perp$ is far from 1. That is, given a fixed ε_{avg}, the lowest exciton binding energy increases with increasing anisotropy, as the lowest state wave function deviates from the isotropic $1s$ wave function. As expected, larger effective masses result in larger exciton binding energies and smaller exciton radii.

B. Electroabsorption

Electroabsorption and electroreflection studies have provided considerable information about band and localized states in both organic and inorganic semiconductors.[28–30,53–57] Localized states in molecular crystals result in comparatively smaller electric-field effects than in inorganic semiconductors, where the low exciton binding energy (~10 meV) can be strongly perturbed by even small external fields. Hence, in molecular crystals, the first- and second-order Stark effects are interpreted in the context of a local dipole moment interacting with a local electric field.[11,53] For tightly bonded (~1 eV) Frenkel excitons, the change of absorption follows the first derivative of the absorption with respect to energy,[54] and for polar CT excitons with large transition dipoles and with binding energies ≤500 meV, the change of absorption is proportional to the second derivative of the absorption spectrum.[11,55]

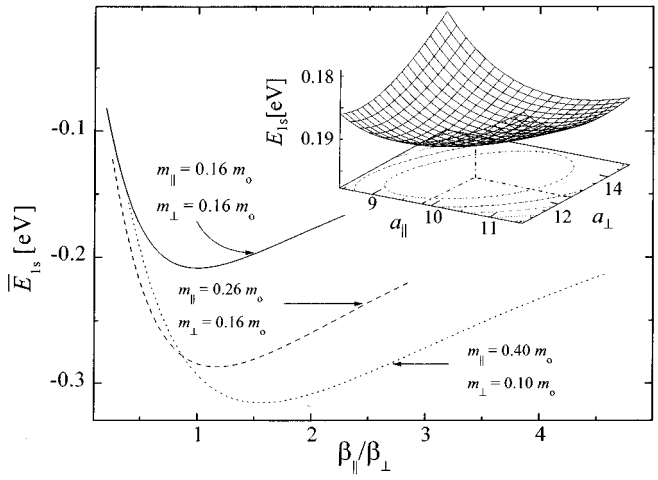

FIG. 7. Minimum energy of the $1s$-like exciton state ($\overline{E_{1s}}$) as a function of anisotropy ($\beta_\parallel/\beta_\perp$) for different reduced effective masses. Inset: $2D$ plot of $E(a_\parallel, a_\perp)$ as a function of $a_\parallel$ and $a_\perp$. The calculation is done with $m_\parallel = m_\perp = 0.18m_0$, and $\vec{\varepsilon}$ is obtained using Eq. (18). The minimum energy $\overline{E_{1s}^{(0)}} = (191 \pm 20)$ meV (indicated by a dashed line), corresponds to $\overline{a_\parallel} = (9.8 \pm 0.3)$ Å and $\overline{a_\perp} = (12.5 \pm 0.2)$ Å.

However, organic systems containing extended, conjugated bonds have been suspected of having wide energy bands.[56,57] Furthermore, molecular systems with closely stacked π orbitals may also have sufficient overlap to support delocalized exciton states, such that their EA spectrum needs to be considered as a perturbation of these delocalized states. For example, electroreflectance studies of the $\pi-\pi^*$ excitations of the poly-diacetylene single crystal poly-1,6-di(N-carbazolyl)-2,4-hexadiynel shows an extended CT exciton state whose EA response is ten times larger than for the localized Frenkel exciton lines in that same material.[54,55]

The EA spectrum due to excitons in crystalline thin films of PTCDA has been previously studied.[28] In that work, the EA transmission spectra were measured at room temperature, where the peak amplitude of the sinusoidal field varied from $F=|\mathbf{F}|=100$–300 kV/cm. In that work, we observed a quadratic dependence of the change of absorption ($\Delta\alpha$) on F, shown in Fig. 8. Given the Hamiltonian H_0 along with the basis wave functions φ_n provided in Eqs. (20) and (21), we can fit the data using

$$H=H_0+H_1, \tag{22a}$$

where H_1 is the potential energy due to the applied field. However, since an external field $\mathbf{F}_0$ will polarize the crystal, the local field $\mathbf{F}_{\rm loc}$ on the exciton and the macroscopic field $\mathbf{F}_{\rm mac}$ in the crystal may be different. It can be shown (Appendix A 1) that

$$H_1=q\int_{r_e}^{r_h}\mathbf{F}_{\rm loc}\cdot d\mathbf{r}=q\mathbf{F}_{\rm mac}\cdot\mathbf{r}. \tag{22b}$$

At low electric fields (i.e., $qFa_{\rm avg}=q|\mathbf{F}|a_{\rm avg}<E_{1s}^{(0)}\approx 200$ meV, or $F<2$ MV/cm, where $a_{\rm avg}=\sqrt[3]{\overline{a_\perp}\,\overline{a_\parallel^2}}\approx 11$ Å), H_1 can be treated as a perturbation to H_0. Using the trial wave function[58]

$$\psi_{1s}=\varphi_{1s}\left\{1-\frac{2H_1\varepsilon_{\rm avg}a_{\rm avg}}{q^2}\,(1+g_{1s}/2)\right\}, \tag{23}$$

the energy shift is thus found for a field oriented in the normal and in-plane ($i=\perp$, $\parallel$, respectively) directions, as

$$\Delta E=E_{1s}-E_{1s}^{(0)}=-\tfrac{9}{4}\varepsilon_{\rm avg}F_i^2\overline{a_i^2}a_{\rm avg}. \tag{24}$$

Also, the broadening of the state due to the external field is given by

$$\langle H_1^2\rangle=\langle(q\mathbf{F}_{\rm mac}\cdot\mathbf{r})^2\rangle=q^2F_i^2\overline{a_i^2}. \tag{25}$$

The ratio of shifting to exciton line broadening is therefore *independent of crystal direction*:

$$\Delta E/\langle H_1^2\rangle=-\varepsilon_{\rm avg}a_{\rm avg}9/4q^2. \tag{26}$$

Therefore, in the limit of small fields, the change of the exciton absorption spectrum depends quadratically on the electric field, via

$$\Delta\alpha(\mathbf{F},E_{\rm ph})=\frac{\partial\alpha(E_{\rm ph})}{\partial E_{\rm ph}}\,\Delta E+\frac{\partial^2\alpha(E_{\rm ph})}{\partial E_{\rm ph}^2}\,\langle H_1^2\rangle+\cdots, \tag{27}$$

where $E_{\rm ph}$ is the photon energy. The quadratic dependence [Eqs. (24)–(27)] is shown in the inset of Fig. 8 for PTCDA,

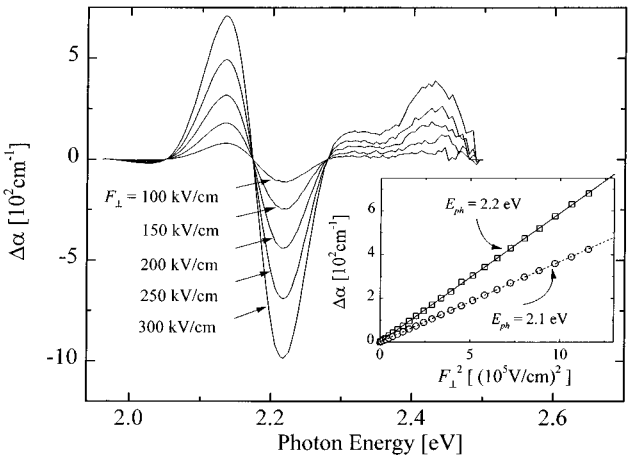

FIG. 8. Room-temperature PTCDA electroabsorption ($\Delta\alpha$) spectra at various electric fields oriented normal to the substrate $F_\perp$. Inset: Electroabsorption magnitude as a function of $F_\perp^2$ at two different photon energies, $E_{\rm ph}=2.1$ and 2.2 eV.

where the electric field is applied along $\perp$, and $\Delta\alpha$ is measured at photon energies: $E_{\rm ph}=2.1$ and 2.2 eV. The EA spectra at various electric fields oriented along different directions are also plotted in Figs. 8 and 9.

The lowest energy absorption peak at (2.23 ± 0.03) eV in the PTCDA spectrum has previously been associated unambiguously with a spatially extended CT state, whereas the higher-energy absorption peaks correspond to Frenkel exciton absorption.[14] Due to the localized nature of the Frenkel excitons, these latter states are less sensitive to the applied electric field due to their small spatial extent.[55] Furthermore, since the Frenkel excitons respond to the electric via the change in polarizability, the EA spectra of such states are proportional to the first derivative of absorption[11] $\partial\alpha/\partial E$. Hence the high-energy features (>2.3 eV in PTCDA) exhibit a smaller electric-field dependence and different line shape as compared to the low-energy CT states. From Figs. 8 and 9, therefore, we conclude that the EA spectrum measured for PTCDA is primarily due to line broadening of the lowest-energy CT state.

Hence $\Delta\alpha$ is fit using two parameters ΔE and $\langle H_1^2\rangle$, while $\partial\alpha/\partial E$ and $\partial^2\alpha/\partial E^2$ are obtained from the lowest, inhomogeneously (phonon) broadened CT absorption line which is accurately approximated by a single Gaussian[14] (lower dashed line of Fig. 9) with a peak energy of (2.23 ± 0.03) eV and a width of (0.17 ± 0.02) eV. According to Eq. (26), broadening dominates the EA spectra due to the small exciton radius $[\Delta E/\langle H_1^2\rangle\sim-0.14\pm0.02\ \ (10^5\ \text{V/cm})^2/(\text{meV})^2]$. Thus the ratio $\Delta E/\langle H_1^2\rangle$ is used to estimate $a_{\rm avg}$, while $\langle H_1^2\rangle_\perp/\langle H_1^2\rangle_\parallel$ gives the ratio of the exciton radii along $\perp$ and $\parallel$ directions. Figure 9 shows the EA data and fits for normal and in-plane fields. Due to the large absorption and reduced detector sensitivity energies >2.3 eV, the signal-to-noise ratio was insufficient to resolve any additional EA spectra features at high energies. From these fits, we find, $\overline{a_\perp}=(12.5\pm0.5)$ Å and $\overline{a_\parallel}=(10.2\pm0.4)$ Å (see Table III). Note that the fits in Fig. 9 are improved from those reported previously due to the use of the microscopic Hamiltonian [Eq. (19)] along with our calculation of P_E for PTCDA in Fig. 3.

The small anisotropy found for the PTCDA exciton radii

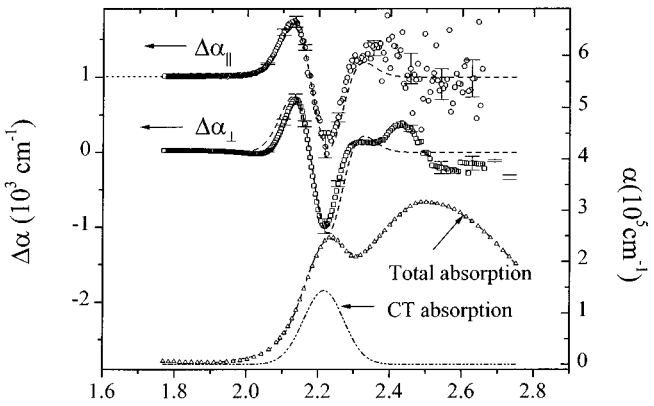

FIG. 9. Absorption (α) and electroabsorption ($\Delta\alpha$) spectra of PTCDA. Top: Electroabsorption spectra and numerical fits (dashed lines) with fitting parameters listed in Table III. For the field oriented parallel to the substrate, the electroabsorption (circles) $\Delta\alpha_\parallel$ was obtained at $F_\parallel = 0.16$ MV/cm, and for perpendicular fields (squares) $\Delta\alpha_\perp$, the field was $F_\perp = 0.15$ MV/cm. Bottom: Absorption spectrum (triangles) and the fit (lines). The fit of the total spectrum assumes a series of Gaussian line shapes corresponding to previously resolved (Ref. 14) exciton line shapes for PTCDA. The dash-dotted line corresponds to the CT absorption component of the fit with a peak energy of (2.23 ± 0.03) eV and a width of 0.17 eV.

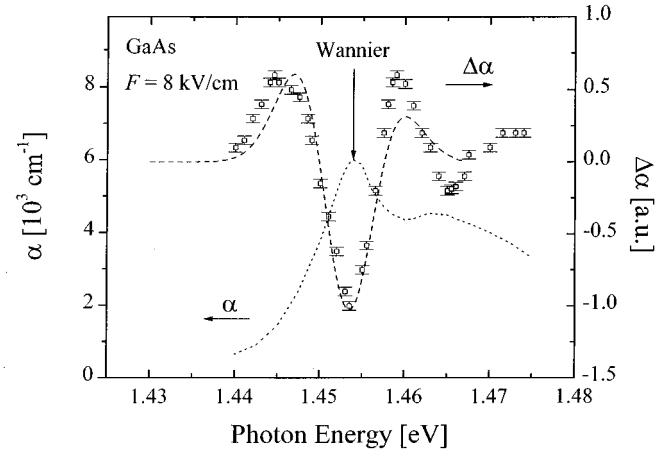

FIG. 10. Top: Fit (dashed line) to the electroabsorption spectrum (squares) of GaAs at $F = 8$ kV/cm taken from Ref. 29 using the theory in text. Bottom: Band-edge absorption spectrum of GaAs indicating the Wannier exciton state. Data are also from Ref. 29.

suggests a similarly small anisotropy in the effective reduced mass. Indeed, we find the effective masses to be $m_\perp = (0.17 \pm 0.01) m_0$ and $m_\parallel = (0.19 \pm 0.01) m_0$, along with an exciton binding energy of $E_{1s} = (185 \pm 20)$ meV (results summarized in Table III). This apparently contradicts previous measurements of the hole mobility,[37] where $\mu_{p,\perp} \approx 10^6 \mu_{p,\parallel}$, suggesting that $m_\perp \ll m_\parallel$. However, we note that the EA measurement provides the so-called ''Coulombic'' effective mass of the nearly symmetric $1s$ state, while the mobility measurements provide the ''transport'' mass inferred from $\mu = q\tau/m$. Clearly, these two measurements can yield very different values for m since $\mu \propto \tau$, where τ is the carrier scattering time. That is, τ can carry the anisotropy in μ due to enhanced scattering along a particular crystalline direction. For the case of PTCDA, the motion of a charge along $\parallel$ is easily scattered by the large intermolecular potential barriers (for example, V_{pseudo} in Fig. 4), leading to strong localization in that direction. Hence, $\tau_\parallel$ is expected to be much less than $\tau_\perp$, leading to the very anisotropic mobility observed, while the effective mass remains largely isotropic, since it is primarily due to the electronic distribution *within* a given molecule.

The analysis of the EA spectra is also valid for Wannier excitons in semiconductors such as GaAs,[29,30] since the theory suggests that both delocalized CT excitons and Wannier states have the same origin described by the Hamiltonian in Eq. (19). In fact, the EA spectrum of PTCDA in Fig. 8 is very similar to that found by Miller *et al.* for GaAs, shown in Fig. 10 (data points). The broadening observed in GaAs was qualitatively attributed, in that work, to field ionization shortening of the exciton lifetime, optical-phonon collisions, etc. However, a more quantitative fit can be achieved using the same wave function and potential employed to describe field-induced line broadening in CT excitons in organic films. Hence in Fig. 10 we show the EA data and a fit starting with the measured exciton absorption spectrum shown by the dotted line in Fig. 10. Our best fit is obtained assuming $a \approx 70$ Å, and $E_{1s} \approx 8$ meV, consistent with expected values for bulk GaAs. The fact that the spectrum can be fit by the same theory applicable to the organic EA spectrum supports the assumption that Wannier and CT excitons have a common physical origin which can be approximated by a hydrogenic wave function broadened in an external electric field. Indeed, to our knowledge, this is the first case where the bulk GaAs EA line shape has been accurately fit by a simple quantum-mechanical model.

Note that for both PTCDA and GaAs, we use the relative values of $\Delta E/\langle H_1^2 \rangle$ and $\langle H_1^2 \rangle_\perp / \langle H_1^2 \rangle_\parallel$ to find the exciton binding energy and radii along the different crystal direc-

TABLE III. Summary of the result for PTCDA.

	Symbol	Unit	EA results	QC results
Exciton binding energy	E_{1s}	meV	185 ± 20	177 ± 20
Exciton radius along the normal direction	$a_\perp$	Å	12.5 ± 0.5	12.9 ± 1.0
Exciton radius along the in-plane direction	$a_\parallel$	Å	10.2 ± 0.4	
Effective reduced mass along the normal direction	$m_\perp$	m_0	0.17 ± 0.02	0.16 ± 0.02
Effective reduced mass along the in-plane direction	$m_\parallel$	m_0	0.19 ± 0.02	

tions. However, the *absolute magnitude* of the measured broadening and the Stark shift as a function of electric field F is ~10 times smaller than expected. We speculate that this discrepancy is primarily due to the strong exciton-phonon coupling leading to substantial equilibrium line broadening which would tend to reduce the observed effects.[59] However, a more quantitative explanation of this discrepancy remains to be developed.

C. Quantum confinement in organic multilayer structures

Evidence of quantum confinement (QC) of extended CT states in organic multilayer structures was previously provided by So and Forrest,[15] Haskal *et al.*,[16] and Hong *et al.*[18] It was observed that the lowest-energy absorption peak,[15,18] the ground-state vibrational frequency[16] of the exciton fluorescence spectra, and the exciton photoluminescence peak[18] shift to higher energies as the layer thickness is decreased. Here we use the Hamiltonian of Eq. (19) to quantitatively study these blueshifts in the lowest-energy (CT) absorption peak in PTCDA.

The blueshift in PTCDA/NTCDA MQW absorption and fluorescence has been attributed[15] to excitons confined by energy discontinuities of the HOMO and LUMO bands at the heterointerfaces between the adjoining organic layers. To fit the shifts, So and Forrest[15] modeled a single PTCDA quantum well sandwiched between NTCDA layers, and a fixed $\overline{a_\perp}$ at 12 Å, along with an isotropic effective mass $m_\parallel = m_\perp = 0.18 m_0$ and dielectric constant $\overline{\varepsilon} = (\varepsilon_\perp + 2\varepsilon_\parallel)/3 = 3.6$. The exciton in-plane radius $\overline{a_\parallel}$ was found to increase monotonically with the increasing well width (d), and it asymptotically approaches the free exciton Bohr radius of 12 Å as $d \gg \overline{a_\parallel}$. Here we take a more rigorous and general approach by using the Hamiltonian in Eq. (19), and allowing the effective mass to be anisotropic and discontinuous across the heterointerfaces.

The Hamiltonian of an e-h in the multiple quantum-well structure is

$$H = T_\parallel + T_{e,\perp} + T_{h,\perp} + V_{e\text{-}h} + V_e(z_e) + V_h(z_h), \qquad (28)$$

where $T_\parallel$ is the in-plane kinetic energy, $T_\parallel = (-\hbar^2/2m_{e\text{-}h,\parallel})\nabla_\parallel^2$, $m_{e\text{-}h,\parallel}$ is the reduced mass along $\parallel$, and $T_{e,\perp} = (-\hbar^2/2m_{e,\perp})(\partial^2/\partial z_e^2)$ and $T_{h,\perp} = (-\hbar^2/2m_{h,\perp})(\partial^2/\partial z_h^2)$ are the kinetic energies along the normal direction with corresponding masses $m_{e,\perp}$ and $m_{h,\perp}$. Also, z_e and z_h are the normal coordinates for the electron and hole, respectively, $V_{e\text{-}h}$ is obtained from Eq. (17), and V_e and V_h are the LUMO and HOMO levels (inset Fig. 11). For multilayers consisting of PTCDA and NTCDA, the offsets of the LUMO and HOMO energy-band minima were found[15] to be $\Delta E_{\mathrm{LUMO}} = 980$ meV and $\Delta E_{\mathrm{HOMO}} = 50$ meV (where NTCDA has the larger HOMO-LUMO energy gap). For simplicity, we only consider QC of the lowest, nearly symmetric $1s$ CT state corresponding to the lowest-energy absorption peak observed in the PTCDA spectrum.

The inset of Fig. 11 shows a symmetric MQW with a periodicity of $2d$. Here, $N = 0, \pm 1, \pm 2, \ldots$ denotes the number of the multilayers, where even numbers are for the quantum-well (PTCDA) regions, and odd numbers are for the barrier (NTCDA) regions. Since $\Delta E_{\mathrm{LUMO}} \gg \Delta E_{\mathrm{HOMO}}$,[15]

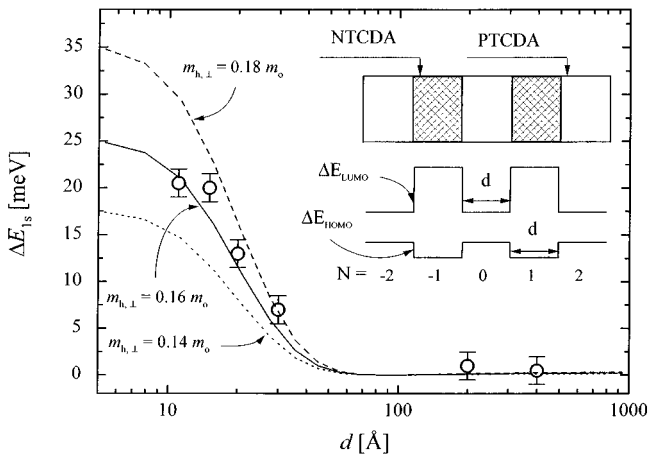

FIG. 11. Energy shift of the PTCDA CT absorption peak ΔE as a function of PTCDA layer thickness d. The symbols correspond to the experimental data, and the solid curve is the fit using $m_{h,\perp} = 0.16 m_0$. The fit is also compared with the dashed curve using $m_{h,\perp} = 0.18 m_0$, and the dotted line using $m_{h,\perp} = 0.14 m_0$. Inset: Schematic diagram of the quantum-well structure consisting of alternating PTCDA and NTCDA layers of equal thickness. Here N is the layer index.

and $m_e \gg m_h$, the electron is approximated as confined in layer $N = 0$ of infinite depth. For a hole in layer N (where $z_h \in [Nd - d/2,\ Nd + d/2]$), the trial wave function of the lowest exciton state can be written as the product of the free-exciton wave function $[\varphi_{e\text{-}h}(\rho, z = z_h - z_e)]$, and the electron $[\varphi_e(z_z)]$ and hole $[\varphi_h(z_h)]$ envelope functions. These later two functions are oscillatory in the wells, and decaying in the barriers (see Appendix A 2):

$$\psi = A(N)\cos(\pi z_e/d) \times \begin{cases} \cos[k(z_h - Nd)]\exp(-g) & N \in \text{even} \\ \dfrac{\cos(kd/2)\cosh[\kappa(z_h - Nd)]}{\cosh(kd/2)}\exp(-\gamma g) & N \in \text{odd}, \end{cases} \qquad (29)$$

with $\gamma = m_{h,b,\perp}/m_{h,w,\perp}$, and where $m_{h,w,\perp}$ and $m_{h,b,\perp}$ are the effective hole masses along the z direction in the well and barrier regions, respectively. Also, k and κ are obtained via

$$H_h\varphi_h = [T_{h,\perp} + V_h(z_h)]\varphi_h = E_h\varphi_h . \qquad (30)$$

Minimizing $E_{1s}(a_\parallel, a_\perp) = \langle\psi|H|\psi\rangle$, we fit the absorption peak shift data obtained by So and Forrest[15] in multilayer structures, such that an independent estimate of exciton radius and reduced mass can be compared with values found from the EA measurements (see Sec. III B). The detailed treatment of variational minimization of the exciton energy in MQWs is provided in Appendix A 3.

Using $m_{h,\perp} = 0.16 m_0$ (listed in Table III), we fit the 25 meV blueshift observed as the well width d decreases from 500 to 3 Å (solid curve, Fig. 11). The results obtained for different hole masses are also shown for comparison in Fig. 11, where the dashed curve corresponds to $m_{h,\perp} = 0.18 m_0$ and the dotted line corresponds to $m_{h,\perp} = 0.14 m_0$. We find that the blueshift of the exciton energy vs d tapers off for

$d<10$ Å due to the onset of tunneling between wells, in which case the holes are no longer further confined as $d\rightarrow 0$. This condition corresponds to that observed for multiple organic bilayers recently reported by Hong *et al.*[18]

Thus the estimated effective mass along the normal direction measured using the absorption blueshift data in PTCDA/NTCDA MQW's is consistent with the results obtained from fitting the EA data for homogeneous PTCDA thin films (see Table III). The consistency shows the validity of describing a CT exciton using hydrogenic wave functions, and therefore suggests that Wannier states in inorganic semiconductors and CT excitons in such tightly stacked nonpolar vdW-bonded organic crystals have essentially the same physical origin. This observation is similar to the case of the transition of Frenkel to Wannier excitons previously observed in pressurized fluid xenon.[60] Furthermore, the narrowing of the optical bandgap of PTCDA under hydrostatic pressure[41] supports the delocalized picture for the CT exciton in this material. These data provide conclusive evidence that Wannier-like CT excitons exist in molecular compounds characterized by closely spaced planar molecules, resulting in a large molecular wave-function overlap between adjacent molecules leading to extended (Block-like) electronic states.

D. Stark shifts and spectral broadening in organic MQW's

In previous work,[61] the Stark shift in organic MQW's was calculated. The exciton ground-state energy shift for various quantum-well configurations was found to be similar to the bulk values. However, line broadening was not considered, although we saw from the previous discussion that this plays an important role in determining the EA spectra.[28] We briefly showed quantum confinement effects on the broadening in the context of the Hamiltonian in Eq. (19).

In Eq. (25), it was found that the broadening is proportional to the exciton radius. For the electric field oriented along $\perp$, the ratio of line broadening for the confined versus the free exciton is

$$\xi=\langle\psi|z^2|\psi\rangle/\langle\varphi|z^2|\varphi\rangle \tag{31}$$

where ψ is the wave function for confined states [Eq. (29)], and φ is the free $1s$ exciton state [Eq. (21)]. Using $m_{\parallel}=m_{\perp}=0.16m_0$ and $\varepsilon_{\text{avg}}=3.2$, we calculate the broadening ratio for two different HOMO-LUMO energy barrier offsets ($\Delta E_{\text{HOMO}}=50$ and 550 meV) with the result shown in Fig. 12. As expected, for thick wells [$d/a_{\text{eff}}\rightarrow\infty$, where a_{eff} is defined in Appendix A 3 as the free-exciton radius $a_{\text{eff}}=\overline{a_{\perp}}(d\rightarrow\infty)$], the broadening is not affected by the quantum well. As d decreases, the broadening decreases with the exciton radius as the exciton is ''squeezed'' by the barrier layers, where a larger barrier height results in a larger confinement (therefore, smaller broadening), as one would expect. However, as d decreases further, tunneling between layers becomes significant. In this case, the exciton radius increases with respect to decreasing d, eventually reaching its bulk value for $d\rightarrow 0$.

Thus we conclude that multiple quantum wells can reduce the CT line broadening at some optimized well width d_{opt}: the larger the barrier energy, the smaller the broadening. However, since the magnitude of the EA depends on both shift and broadening, the reduced broadening in MQW's will result in a smaller, total EA effect.

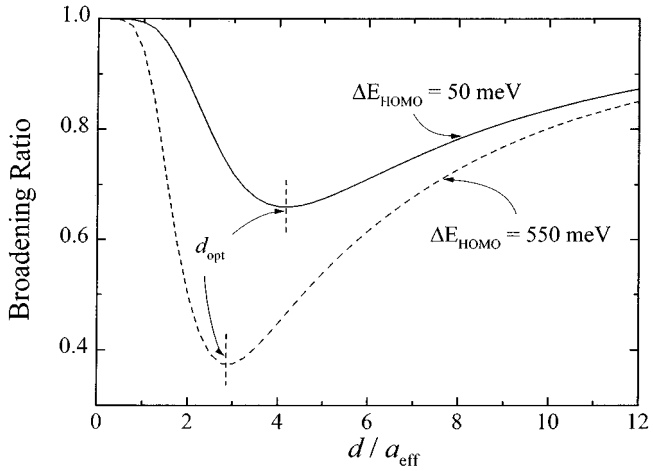

FIG. 12. The ratio of CT exciton line broadening in a MQW to the broadening in bulk, as a function of the reduced well width d/a_{eff}. Here $a_{\text{eff}}=\varepsilon_{\text{avg}}\hbar^2/mq^2$, which equals the exciton radius for bulk material. For simplicity, this calculation assumes an isotropic effective mass and a dielectric tensor, such that a_{eff} is not sensitive to orientation. Two values of the HOMO offset, $\Delta E_{\text{HOMO}}=50$ and 550 meV, are assumed. A larger HOMO offset results in a larger change in the broadening.

IV. CONCLUSIONS

We develop a method to treat CT excitons analytically in tightly packed neutral molecular crystals, which accurately describes several different spectroscopic features of organic nanostructures. Starting from a calculation of the polarization energy in anisotropic organic crystals, we derive the electron-hole interaction potential, and confirm the validity of approximating the organic crystal by a quasimacroscopic polarizable medium specified by an effective dielectric tensor $\vec{\varepsilon}(\mathbf{r})$. We find that for organic crystals with a large overlap between the orbitals in adjacent molecules, the CT charge pair becomes delocalized, resulting in a crystalline pseudopotential smaller than the energy bandwidth. In this case, the CT exciton can be accurately represented by a hydrogenlike wave function.

Using a Hamiltonian modified to account for the calculated molecular polarization, and using the resulting hydrogenic trial wave functions, we are able to accurately fit the electroabsorption data for homogeneous PTCDA thin films, as well as the absorption spectral shifts observed in PTCDA-based multiple quantum wells. The analyses of such experiments give independent and consistent estimations of the exciton radii for PTCDA along different crystal axes. A nearly spatially symmetric CT exciton with a radius of $\sim$11 Å (and an eccentricity of $a_{\parallel}/a_{\perp}=0.8$) is found, which corresponds to the observation of a nearly isotropic effective mass. We successfully extend this treatment to other exciton systems found in a wide range of interesting neutral organic molecular and inorganic semiconductors (such as GaAs), suggesting that Wannier and CT excitons have a common physical origin which can be approximated by a hydrogenic wave function. This work provides conclusive evidence that PTCDA

and similarly close-packed molecular compounds represent a class of materials that share many properties with both conventional semiconductors and insulatorlike organic molecular crystals.

In summary, the primary finding of this work is the common physical origin of Wannier and CT excitons in closely packed organic molecular crystals. While the results of this work can be easily generalized to explain a variety of observations of the optical properties relating to the layer thickness or aggregate size of both organic and inorganic nanostructures, we provide an interesting viewpoint with which to consider van der Waals-bonded solids represented by the archetypal compound PTCDA. The broad and rich range of physics developed for understanding quantum confinement in inorganic semiconductors which has ultimately lead to the precise control and manipulation of their densities of states to attain desired optoelectronic properties, appear to be equally applicable to organic nanostructures, provided there is a sufficiently large degree of charge delocalization resulting from details of the crystal structure. In that sense, ''transitional'' materials such as PTCDA and related compounds have bridged the gap between highly delocalized semiconducting systems, and insulators.

ACKNOWLEDGMENTS

The authors acknowledge support for this work from the Air Force Office of Scientific Research and the National Science Foundation. We also thank V. Bulovic for helpful discussions.

APPENDIX

1. Screening of a position-independent external field

Given an e-h pair with a position-independent external field $\mathbf{F}_0$, we take the Fourier transformation over a periodic crystal lattice to obtain

$$\mathbf{F}_0(\mathbf{y})=\sum_l \mathbf{F}_0\exp[2\pi i\mathbf{y}\cdot\mathbf{r}(lkk')]=1/\nu\mathbf{F}_0\delta(\mathbf{y}). \quad \text{(A1)}$$

The polarization response of the crystal in Fourier space is then

$$\begin{aligned}p_E(\mathbf{y})=&\sum_{k_ak_b}[\mathbf{F}_e(-\mathbf{y},k_ak_e)+\mathbf{F}_h(-\mathbf{y},k_ak_h)+\mathbf{F}_0(-\mathbf{y})]^T\\&\times\vec{\Theta}(k_ak_b)\cdot[\mathbf{F}_e(\mathbf{y},k_bk_e)+\mathbf{F}_h(\mathbf{y},k_bk_h)+\mathbf{F}_0(\mathbf{y})]\\=&p_{E,e\text{-}h}(\mathbf{y})+p_{E,F}(\mathbf{y})+\Delta p(\mathbf{y}),\end{aligned} \quad \text{(A2)}$$

where $p_{E,e\text{-}h}$ corresponds to the polarization response due to the e-h pair, $p_{E,F}$ is the polarization response to the external field $\mathbf{F}_0$, while Δp is due to the coexistence of both the e-h pair and $\mathbf{F}_0$, and can be viewed as the contribution to $V_{e\text{-}h}$ due to the external field, or the contribution to the external field potential corrected by the e-h pair screening:

$$\begin{aligned}\Delta p(y)=&\sum_{k_ak_b}\{[\mathbf{F}_e(-\mathbf{y},k_ak_e)+\mathbf{F}_h(-\mathbf{y},k_ak_h)]^T\cdot\overline{\Theta}(k_ak_b)\\&\cdot\mathbf{F}_0(\mathbf{y})+\mathbf{F}_0(-\mathbf{y})^T\cdot\vec{\overline{\Theta}}(k_ak_b)\\&\cdot[\mathbf{F}_e(\mathbf{y},k_bk_h)+\mathbf{F}_h(\mathbf{y},k_bk_h)]\}.\end{aligned} \quad \text{(A3)}$$

Here $\mathbf{F}_e$ is the field induced by the electron

$$\begin{aligned}\mathbf{F}_e(\mathbf{y},kk_e)=&-q\lim_{r\to r(l_ek_e)}\sum_l\exp[2\pi i\mathbf{y}\cdot\mathbf{r}(lk,l_ek_e)]\\&\times\nabla|\mathbf{r}(lk)-\mathbf{r}|^{-1},\end{aligned} \quad \text{(A4)}$$

with a similar expression for the field induced by holes $\mathbf{F}_h$. Now Δp is nonzero for the regions near $y\to0$, where[12]

$$\mathbf{F}_e(\mathbf{y},kk_e)\to-(i2q/\nu)\mathbf{y}/|\mathbf{y}|^2. \quad \text{(A5)}$$

Noting that the external field is irrotational (i.e., $\mathbf{F}_0\times y=0$), we have

$$\begin{aligned}\Delta p\to&\sum_{k_ak_b}\left\{-\frac{4q\ \sin(\pi\mathbf{y}\cdot\mathbf{r})}{|\mathbf{y}|^2\nu}[\mathbf{y}\cdot\overline{\Theta}(\mathbf{y},k_ak_b)\cdot\mathbf{F}_0(\mathbf{y})\right.\\&\left.+\mathbf{F}_0(-\mathbf{y})\cdot\vec{\overline{\Theta}}(\mathbf{y},k_ak_b)\cdot\mathbf{y}]\right\}\\\to&(-8\pi q/\nu^2)\sum_{k_ak_b}[\mathbf{y}\cdot\overline{\Theta}(\mathbf{y},k_ak_b)\cdot\mathbf{y}]\\&\times(\mathbf{F}_0\cdot\mathbf{y})\delta(\mathbf{y})/|\mathbf{y}|^2.\end{aligned} \quad \text{(A6)}$$

Integrating over y then yields the total polarization energy ΔP due to the coexistence of the e-h pair and the external field, via

$$\Delta P=-\frac{\nu}{2}\int_{bz}d\mathbf{y}\ \Delta p\to(-q\mathbf{F}_0\cdot\mathbf{r})\left(1-\frac{1}{\varepsilon_{\text{avg}}}\right), \quad \text{(A7)}$$

where we define the spatial average dielectric constant as $3/\varepsilon_{\text{avg}}=1/\varepsilon_\perp+2/\varepsilon_\parallel$. Note that the macroscopic electric field is $F_{\text{mac}}=E_0/\varepsilon_{\text{avg}}=V/d$, where V is the applied potential across the organic film of thickness d. The potential at the e-h pair due to the external field is then

$$H_1=q\mathbf{E}_0\cdot\mathbf{r}+\Delta P\to(q\mathbf{E}_0\cdot\mathbf{r})/\varepsilon_{\text{avg}}=q\mathbf{F}_{\text{mac}}\cdot\mathbf{r}. \quad \text{(A8)}$$

The external field is therefore screened by the spatially averaged dielectric constant ε_{avg} as a result of the polarization of the ionic displacement of the crystal.

2. Trial wave function for excitons in a multiple-quantum-well structure

For a symmetric MQW with periodicity $2d$, the trial wave function is

$$\psi(\rho,\theta,z_h,z_e)=\varphi_e(z_e)\varphi_h(z_h)\varphi_{e\text{-}h}(\rho,\theta,z=z_h-z_e), \quad \text{(A9)}$$

while the electron and hole potentials are nonzero in the barrier regions [i.e., $V(z_h)=\Delta E_{\text{HOMO}}$ and $V(z_e)=\Delta E_{\text{LUMO}}$], and are zero in the well regions. In PTCDA/NTCDA multilayers, $\Delta E_{\text{LUMO}}\gg\Delta E_{\text{HOMO}}$,[15] and $m_e\gg m_h$, and the electron

is thus approximated as confined in layer $N=0$ of infinite depth. Therefore, for the lowest-energy state, we have

$$\varphi_e(z_z)=\begin{cases}\cos(\pi_0 z_e/d) & |z_e|\leqslant d/2\\ 0 & |z_e|>d/2\end{cases}, \tag{A10a}$$

$$\varphi_h(z_h)=\begin{cases}\cos[k(z_h-Nd)] & N\in\text{even}\\ \dfrac{\cos(kd/2)\cosh[\kappa(z_h-Nd)]}{\cosh(kd/2)} & N\in\text{odd},\end{cases} \tag{A10b}$$

$$\varphi_{e\text{-}h}(\rho,z=z_h-z_e)=A(N)\exp(-g_N), \tag{A10c}$$

where $g_N=[\rho^2/a_{\parallel,N}^2+(z_h-z_e)^2/a_{\perp,N}^2]^{1/2}$ is a function of the variational parameters $a_\parallel$ and $a_\perp$, and subscript N denotes the layer index. Since hole masses are different in the different layers, this leads to concomitant differences in $a_\parallel$, $a_\perp$, and g. Assuming that the wave function and mass flux across the heterointerfaces are continuous, we determine the energies and wave functions. At the boundary of layer $N=|2N'|$ and $|2N'|+1$, $z_h=(|2N'|+1/2)d$, we have

$$\begin{aligned}&A(|2N'|)\cos\left(\frac{kd}{2}\right)\exp\{-g_{|2N'|}[z=(|2N'|+1/2)d]\}\\&\quad=A(|2N'+1|)\cosh(\kappa d/2)\\&\qquad\times\exp\{-g_{|2N'|+1}[z=(|2N'|+1/2)d]\}\end{aligned} \tag{A11a}$$

and

$$\hbar^2k^2/2m_{h,|2N'|,\perp}=\Delta E_{\text{HOMO}}-\hbar^2\kappa^2/2m_{h,|2N'+1|,\perp}, \tag{A11b}$$

with

$$\begin{aligned}&\frac{k}{m_{k,|2N'|,\perp}}\tan\left(\frac{kd}{2}\right)-\frac{\kappa}{m_{h,|2N'|+1,\perp}}\tanh\left(\frac{\kappa d}{2}\right)\\&\quad=-\frac{d}{2}\left\{\frac{1}{m_{h,|2N'|,\perp}a_{|2N'|,\perp}^2 g_{|2N'|}[z_h=(|2N'|+\frac{1}{2})d]}\right.\\&\qquad\left.-\frac{1}{m_{h,|2N'|+1,\perp}a_{|2N'|+1,\perp}^2 g_{|2N'|+1}[z_h=(|2N'|+\frac{1}{2})d]}\right\}.\end{aligned} \tag{A11c}$$

Here $m_{h,N,\perp}$ is the effective hole mass in layer N. To make k and κ independent of the in-plane coordinates (ρ,ϕ), and z_e in solving Eq. (A11), the right-hand side of Eq. (A11c) should be zero for all $\mathbf{r}$. This is only possible when

$$a_{|2N'|+1,i}=a_{|2N'|,i}/\gamma=a_i/\gamma, \tag{A12}$$

where $r=m_{h,|2N'|+1,\perp}/m_{h,|2N'|,\perp}$, and i stands for directions $\parallel$ and $\perp$. Thus we have $g_{|2N'+1|}=rg_{|2N'|}=\gamma g$. Hence

$$A(N)=D\prod_{h=1}^{|N|}\exp\{(-1)^h(1+\gamma)g(\rho,z=hd-d/2)\}, \tag{A13}$$

where D is the normalization constant. Hence the wave function for a hole in layer N depends on only two parameters $a_\parallel$ and $a_\perp$, such that

$$\psi=A(N)\begin{cases}\cos(\pi z_e/d)\cos[k(z-Nd)]\exp(-g) & N\in\text{even}\\ \cos\left(\dfrac{\pi z_e}{d}\right)\dfrac{\cos(kd/2)\cosh[\kappa(z-Nd)]}{\cosh(kd/2)}\exp(-\gamma g) & N\in\text{odd}.\end{cases} \tag{A14}$$

3. Variational minimization of exciton energy in ultrathin layers and MQW's

Shinozuka and Matsuura[52] calculated the $1s$ state energy for excitons in a single quantum well with an infinite barrier height using the following trial wave function:

$$\psi=\cos(\pi z_e/d)\cos(\pi z_h/d)\exp(-g), \tag{A15}$$

where g is defined in Eq. (21b). Now the kinetic-energy operator for electrons in the direction perpendicular to the plane of the quantum wells ($T_{e,\perp}$) leads to

$$\frac{T_{e,\perp}\psi}{\psi}=-\frac{\hbar^2}{2m_{e,\perp}}\left(-\frac{\pi^2}{d^2}+\frac{\partial^2\ln\varphi_{e\text{-}h}}{\partial z_e^2}+2\frac{\partial\ln\varphi_e}{\partial z_e}\frac{\partial\ln\varphi_{e\text{-}h}}{\partial z_e}\right), \tag{A16}$$

where similar expressions can be obtained for holes, $T_{h,\perp}$. Since $\varphi_{e\text{-}h}$ is an even function of $z=z_h-z_e$, its first derivative is odd, and its second derivative is even, such that

$$\frac{T\psi}{\psi}=\frac{\hbar^2\pi^2}{2m_\perp d^2}-\frac{\hbar^2}{2m_\perp}\frac{\partial^2\ln\varphi_{e\text{-}h}}{\partial z^2}+H_{\text{cross}}, \tag{A17a}$$

where the $\perp$ reduced mass is $m_\perp=(1/m_{h,\perp}+1/m_{e,\perp})^{-1}$, and

$$H_{\text{cross}}=\frac{\pi}{d}\frac{\partial\ln\varphi_{e\text{-}h}}{\partial z}\left[\frac{\hbar^2}{m_{h,\perp}}\sin\left(\frac{\pi z_h}{d}\right)-\frac{\hbar^2}{m_{e,\perp}}\sin\left(\frac{\pi z_e}{d}\right)\right]. \tag{A17b}$$

Note that $\partial\ln\varphi_{e\text{-}h}/\partial z$ is an odd function of $z=z_h-z_e$. Hence the term $\langle H_{\text{cross}}\rangle=\langle\psi|H_{\text{cross}}|\psi\rangle$ is nonzero even when $m_{h,\perp}=m_{e,\perp}$, and therefore cannot be ignored.

To compare with previous results,[52] we minimize $\langle\psi|H|\psi\rangle$ with respect to parameters $a_\parallel$ and $a_\perp$, assuming an isotropic effective mass and dielectric constant. Using the effective Bohr radius $a_{\text{eff}}=\varepsilon_{\text{avg}}\hbar^2/mq^2$ as the length unit, and the effective Rydberg energy $\text{Ryd}_{\text{eff}}=mq^4/2\varepsilon_{\text{avg}}^2\hbar^2$ as the energy unit, the reciprocal values of $\overline{a_\parallel}$ and $\overline{a_\perp}$ which give the lowest energy are plotted in Fig. 13 (solid curves), and

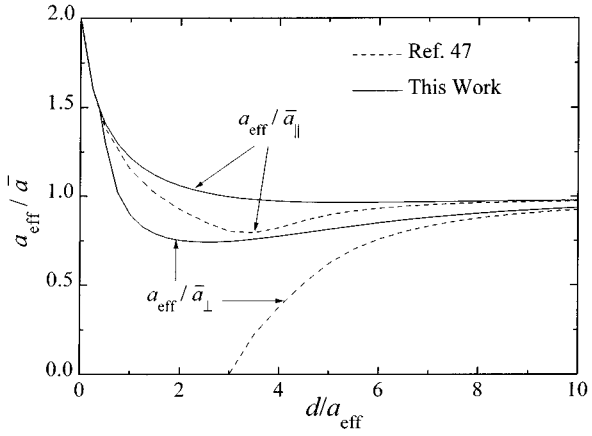

FIG. 13. Values of the variational parameters, $a_{\rm eff}/\overline{a_{\parallel}}$ and $a_{\rm eff}/\overline{a_{\perp}}$, that result in the lowest energy as functions of MQW reduced well width $d/a_{\rm eff}$ (solid lines). These results are compared with those of Ref. 52 (dashed lines).

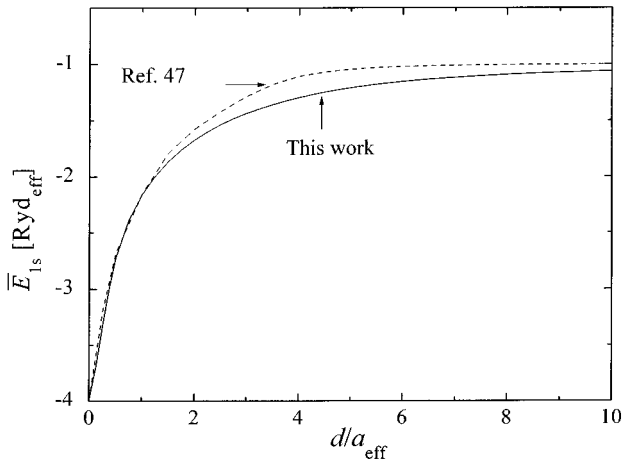

FIG. 14. The exciton binding energy $\overline{E^B_{1s}}=\min_{a_{\parallel},a_{\perp}}\langle\psi|H|\psi\rangle-(\pi^2\hbar^2/2m_{\perp}d^2)$ as a function of MQW well width. The energy is expressed in units of the effective Rydberg energy $\mathrm{Ryd}_{\rm eff}=mq^4/2\varepsilon^2\hbar^2$, which equals the exciton binding energy for bulk material. Note that the binding energy obtained is lower that of Ref. 52 (dashed lines) for intermediate quantum-well width.

the exciton binding energy $\overline{E^B_{1s}}=\min_{a_{\parallel},a_{\perp}}\langle\psi|H|\psi\rangle-(\pi^2\hbar^2/2m_{\perp}d^2)$ is also plotted in Fig. 14 (solid curve). Note that our results are different from those of Shinozuka and Matsuura, which we reproduce in Figs. 13 and 14 (dashed lines) for comparison by minimizing $\langle\psi|H-H_{\rm cross}|\psi\rangle$.

In the limit of thick layers ($d/a_{\rm eff}\to\infty$), note that $\partial\varphi_e/\partial z_z\to 0$ and $\partial\varphi_h/\partial z_h\to 0$, and therefore $\langle H_{\rm cross}\rangle\to 0$, which is the same result as obtained for the very thin layers ($d/a_{\rm eff}\to 0$). On the other hand, the contribution of $\langle H_{\rm cross}\rangle$ to the total energy is large when d and $a_{\rm eff}$ are comparable [i.e., when $(\partial\varphi_h/\partial z_h)\sim(\partial\varphi_e/\partial z_e)\sim(\partial\varphi_{e\text{-}h}/\partial z)$]. Thus our results and those of Ref. 52 converge in both limits, while including $\langle H_{\rm cross}\rangle$ results in lower energies for intermediate well widths. That is, for thick layers, we find $\overline{E^B_{1s}}=-\mathrm{Ryd}_{\rm eff}$ and $\overline{a_{\parallel}}\approx\overline{a_{\perp}}\to a_{\rm eff}$ as expected for a three-dimensional (3D) free exciton, while for thin layers we find $\overline{E^B_{1s}}=-4\ \mathrm{Ryd}_{\rm eff}$, and $\overline{a_{\parallel}}\to a_{\rm eff}/2$, suggesting a 2D exciton.

Note that, while the exciton radius along $\parallel$ direction is $\overline{a_{\parallel}}$, the exciton radius along the $\perp$ direction depends on both $\overline{a_{\perp}}$ and d, and can be expressed as

$$R_{\perp}=\sqrt{\langle\psi|z^2|\psi\rangle}. \tag{A18}$$

In fact, for thin layers, $R_{\perp}\sim d$, independent of $\overline{a_{\perp}}$.

Omitting $\langle H_{\rm cross}\rangle$ results in the radius along $\parallel$ first increasing, followed by a decrease as the well width d decreases. However, including $\langle H_{\rm cross}\rangle$ results in a lower energy, and monotonically decreasing radii with d along both $\perp$ and $\parallel$, showing clear effects of barrier confinement.

[1] R. Hilsh and R. W. Pohl, Z. Phys. **48**, 384 (1928).
[2] J. Frenkel, Phys. Rev. **17**, 1276 (1931).
[3] G. H. Wannier, Phys. Rev. **52**, 191 (1937).
[4] K. Cho, *Excitons* (Springer-Verlag, New York, 1979).
[5] G. E. Pikus and G. L. Bir, *Symmetry and Deformation Effects in Semiconductors* (Nauka, Moscow, 1972; English translation, Wiley, New York, 1974).
[6] S. Sugano, Y. Tanabe, and H. Kamimura, *Multiplets of Transitions Metal Ions in Crystals* (Academic, New York, 1970).
[7] W. Kohn and J. M. Luttinger, Phys. Rev. **97**, 1721 (1955).
[8] M. Ueta, H. Kanzaki, K. Kobayashi, and Y. Toyozawa, *Excitonic Processes in Solids* (Springer-Verlag, New York, 1986).
[9] E. A. Silinsh and V. Capek, *Organic Molecular Crystals* (American Institute of Physics, New York, 1994).
[10] J. M. Luttinger, Phys. Rev. **102**, 1030 (1956).
[11] L. Sebastian, G. Weiser, and H. Bassler, Chem. Phys. **61**, 125 (1981).
[12] P. J. Bounds and R. W. Munn, Chem. Phys. **44**, 103 (1979).
[13] C. J. Ballhausen, *Introduction to Ligand Field Theory* (McGraw-Hill, New York, 1962).
[14] V. Bulovic, P. E. Burrows, S. R. Forrest, J. A. Cronin, and M. E. Thompson, Chem. Phys. **210**, 13 (1996).
[15] F. F. So and S. R. Forrest, Phys. Rev. Lett. **66**, 2649 (1991).
[16] E. I. Haskal, Z. Shen, P. E. Burrows, and S. R. Forrest, Phys. Rev. B **51**, 4449 (1995).
[17] Y. Hirose, V. Aristov, P. Soukiassian, V. Bulovic, S. R. Forrest, and A. Kahn, Phys. Rev. B. **54**, 13 748 (1996).
[18] H. Hong, M. Tarabia, H. Chayet, D. Davidov, E. Z. Faraggi, V. Avny, R. Neumann, and S. Kirstein, J. Appl. Phys. **79**, 3082 (1996).
[19] S. R. Forrest, M. L. Kaplan, and P. H. Schmidt, J. Appl. Phys. **55**, 1492 (1984).
[20] S. R. Forrest, M. L. Kaplan, and P. H. Schmidt, Ann. Rev. Mater. Sci. **17**, 189 (1987).
[21] F. F. So and S. R. Forrest, Appl. Phys. Lett. **52**, 1341 (1988).
[22] S. Mukamel, A. Takahashi, H. X. Huang, and G. Chen, Science **266**, 250 (1994).
[23] N. Wang, J. K. Jenkins, V. Chernyak, and S. Mukamel, Phys. Rev. B **49**, 17 079 (1994).
[24] H. X. Huang and S. Mukamel, Chem. Phys. Lett. **192**, 417 (1992).
[25] O. Dubovsly and S. Mukamel, J. Chem. Phys. **15**, 9201 (1992).

[26] T. Wagersreiter and S. Mukamel, Chem. Phys. **210**, 171 (1996).
[27] H. Fukutome, J. Mol. Struct. **188**, 377 (1989), and references therein.
[28] Z. Shen, P. E. Burrow, S. R. Forrest, Z. Ziari, and W. H. Steier, Chem. Phys. Lett. **236**, 129 (1995).
[29] D. A. B. Miller, D. S. Chemla, T. C. Damen, A. C. Gossard, W. Wiegmann, T. H. Wood, and C. A. Burrus, Phys. Rev. B **32**, 1043 (1985).
[30] M. Ruff, D. Streb, S. U. Dankowski, T. P. Kiesel, B. Knupfer, M. Kneissl, N. Linder, G. H. Dohler, and U. D. Keil, Appl. Phys. Lett. **68**, 2968 (1996).
[31] L. E. Lyons, J. Chem. Soc. 5001 (1957).
[32] A. Jurgis and E. A. Silinsh, Phys. Status Solidi B **53**, 735 (1972).
[33] P. J. Bounds and W. Siebrand, Chem. Phys. Lett. **75**, 414 (1980).
[34] N. F. Mott and R. W. Gurney, *Electronic Processes in Ionic Crystals* (Clarendon, Oxford, 1940).
[35] H. Haken and W. Schottky, Z. Phys. Chem. **16**, 218 (1958).
[36] Y. Toyozawa, Prog. Theor. Phys. **12**, 421 (1954).
[37] S. R. Forrest, P. E. Burrows, E. I. Haskal, and F. F. So, Phys. Rev. B **49**, 11 309 (1994).
[38] E. I. Haskal, F. F. So, P. E. Burrows, and S. R. Forrest, Appl. Phys. Lett. **60**, 3223 (1992).
[39] J. F. Lam, S. R. Forrest, and G. L. Tangonan, Phys. Rev. Lett. **25**, 1614 (1991).
[40] V. Bulovic and S. R. Forrest, Chem. Phys. Lett. **238**, 88 (1995).
[41] A. Jayaraman, M. L. Kaplan, and P. H. Schmidt, J. Chem. Phys. **82**, 1682 (1984).
[42] J. D. Jackson, *Classical Electrodynamics*, 2nd ed. (Wiley, New York, 1975).
[43] M. Born and K. Huang, *Dynamical Theory of Crystal Lattices* (Oxford University Press, Oxford, 1954).
[44] P. G. Cummins, D. A. Dunmur, R. W. Munn, and R. J. Newham, Acta. Crystallogr. A **32**, 854 (1976).
[45] D. A. Dunmur, Mol. Phys. **23**, 109 (1972).
[46] S. R. Forrest, M. L. Kaplan, P. H. Schmidt, T. Venkatesan, and A. J. Lovinger, Appl. Phys. Lett. **41**, 708 (1982).
[47] P. Fenter, P. E. Burrows, P. Eisenberger, and S. R. Forrest, J. Cryst. Growth **152**, 65 (1995).
[48] D. Y. Zhang, F. F. So, and S. R. Forrest, Appl. Phys. Lett. **59**, 823 (1991).
[49] Y. Q. Shi and F. F. So (private communication).
[50] R. Silbey, J. Jortner, S. A. Rice, and M. T. Vala, J. Chem. Phys. **42**, 733 (1965); **43**, 2925 (1965).
[51] R. W. Lof, M. A. vanVeenendaal, B. Koopmans, H. T. Jonkmand, and G. A. Sawatzky, Phys. Rev. Lett. **68**, 3924 (1992).
[52] Y. Shinozuka and M. Matsuura, Phys. Rev. B **28**, 4878 (1983).
[53] J. H. Meyling and D. A. Wiersma, Chem. Phys. Lett. **20**, 383 (1973).
[54] L. Sebastian and G. Weiser, Chem. Phys. **62**, 447 (1981).
[55] L. Sebastian and G. Weiser, Phys. Rev. Lett. **46**, 1156 (1981).
[56] M. Kertesz, J. Koller, and A. Azman, Chem. Phys. **27**, 273 (1978).
[57] E. G. Wilson, J. Phys. C **8**, 727 (1975).
[58] L. I. Schiff, *Quantum Mechanics* (McGraw-Hill, New York, 1968).
[59] J. D. Dow and D. Redfield, Phys. Rev. **13**, 1633 (1976).
[60] P. Laporte and J. L. Subtil, Phys. Rev. Lett. **45**, 2138 (1980).
[61] Z. Shen and S. R. Forrest, Phys. Rev. B **48**, 17 584 (1993).